Exhumation and uplift of the Shillong plateau and its influence on the eastern Himalayas: New constraints from apatite and zircon (U-Th-[Sm])/He and apatite fission track analyses

Subrata Biswas,[1] Isabelle Coutand,[2] Djordje Grujic,[3] Christian Hager,[4] Daniel Stöckli,[4] and Bernhard Grasemann[5]

Received 24 February 2007; revised 19 June 2007; accepted 11 September 2007; published 25 December 2007.

[1] The Shillong plateau is the only raised topography in the foreland of the Himalayas. Located on the trajectory of the Indian Summer Monsoon (ISM), the plateau perturbs the regional distribution of precipitation. As such, the Shillong plateau-eastern Himalaya-ISM is a unique system to quantify the couplings between climate, tectonics, and erosion. A change in long-term erosion rates along-strike of the Bhutan Himalaya was recently attributed to a climatic modulation due to the uplift of the Shillong plateau. To test this interpretation, it is essential to constrain the timing and rate at which the plateau was uplifted and the amount of partitioning of the India-Asia convergence into the plateau. We used apatite and zircon (U-Th-[Sm])/He and apatite fission track analyses to unravel the thermal histories of 13 basement samples collected along a N-S transect across the central Shillong plateau. We find that (1) the exhumation of the plateau began at least 9–15 Ma ago, (2) its surface uplift was chronologically decoupled from its exhumation and started after ~3–4 Ma at rates of 0.4–0.53 mm/a, (3) the long-term horizontal shortening rate accommodated by the plateau is 0.65–2.3 mm/a, which represents only 10–15% of the India-Asia convergence rate. The uplift of the Shillong plateau did not significantly modify the rock uplift rate in the Bhutan Himalaya, which is consistent with the hypothesis of climatic modulation of the Pliocene erosion, tectonic, and landscape evolution previously documented along this orogenic front. **Citation:** Biswas, S., I. Coutand, D. Grujic, C. Hager, D. Stöckli, and B. Grasemann (2007), Exhumation and uplift of the Shillong plateau and its influence on the eastern Himalayas: New constraints from apatite and zircon (U-Th-[Sm])/He and apatite fission track analyses, *Tectonics*, *26*, TC6013, doi:10.1029/2007TC002125.

[1]Department of Geological Sciences, Jahangirnagar University, Savar, Bangladesh.
[2]UMR-CNRS 8110, Processus et Bilans des Domaines Sédimentaires, Université des Sciences et Technologies de Lille 1, Villeneuve d'Ascq, France.
[3]Department of Earth Sciences, Dalhousie University, Halifax, Nova Scotia, Canada.
[4]Department of Geology, University of Kansas, Lawrence, Kansas, USA.
[5]Center for Earth Sciences, University of Vienna, Vienna, Austria.

0278-7407/07/2007TC002125

1. Introduction

[2] The Shillong plateau and the Mikir Hills in NE India may look imperceptible in front of the mighty Himalaya and Tibetan plateau (Figure 1), but it represents a place of superlatives: two reverse faults which may cut the entire crust and displace the Moho [*Mitra et al.*, 2005] delineate the plateau from the surrounding plains. In the north the Oldham fault was the site of the largest ever recorded intraplate earthquake [*Bilham and England*, 2001; *Oldham*, 1899; *Rajendran et al.*, 2004]; and the Dauki fault in the south juxtaposes Precambrian basement against an up to 18-km-thick Tertiary sedimentary basin, the Sylhet Trough [*Alam et al.*, 2003; *Johnson and Alam*, 1991]. In addition, the Shillong plateau was uplifted recently in geological history, i.e., during the Pliocene, and thus may have affected both the tectonics of the Himalaya further north [*Bilham and England*, 2001; *Grujic et al.*, 2006] and the evolution and spatial distribution of the Indian Summer Monsoon (ISM) [*Bookhagen et al.*, 2005; *Grujic et al.*, 2006]. In fact, owing to the orographic interactions with the ISM, the southern flank of the Shillong plateau is the wettest place on the Earth [*Bookhagen et al.*, 2005] (see also Observations about rainfall at Cherrapunjee, 2006, SSNET-Com Pvt. Ltd., available at http://www.cherrapunjee.com/mrcharts.php).

[3] Constraints on the active convergence across the plateau are still scarce and imprecise and there are no data on the rock uplift, the exhumation and ultimately surface uplift of the plateau. The development of the Shillong plateau has supposedly influenced the eastern Himalayan tectonics by consuming up to one third of the convergence between India and Eurasia according to *Bilham and England* [2001]. Its surface uplift has clearly modified the distribution of monsoonal precipitations along the eastern Himalayas, by forming an orographic barrier to the moisture-bearing winds derived from the Bay of Bengal to the south [*Bookhagen et al.*, 2005; *Grujic et al.*, 2006]. A change in long-term erosion rates along the frontal Bhutan Himalayas to the north (Figure 1), as well as a change in their geomorphologic and recent tectonic evolution were attributed to a climatic change due to the topographic construction of the Shillong plateau

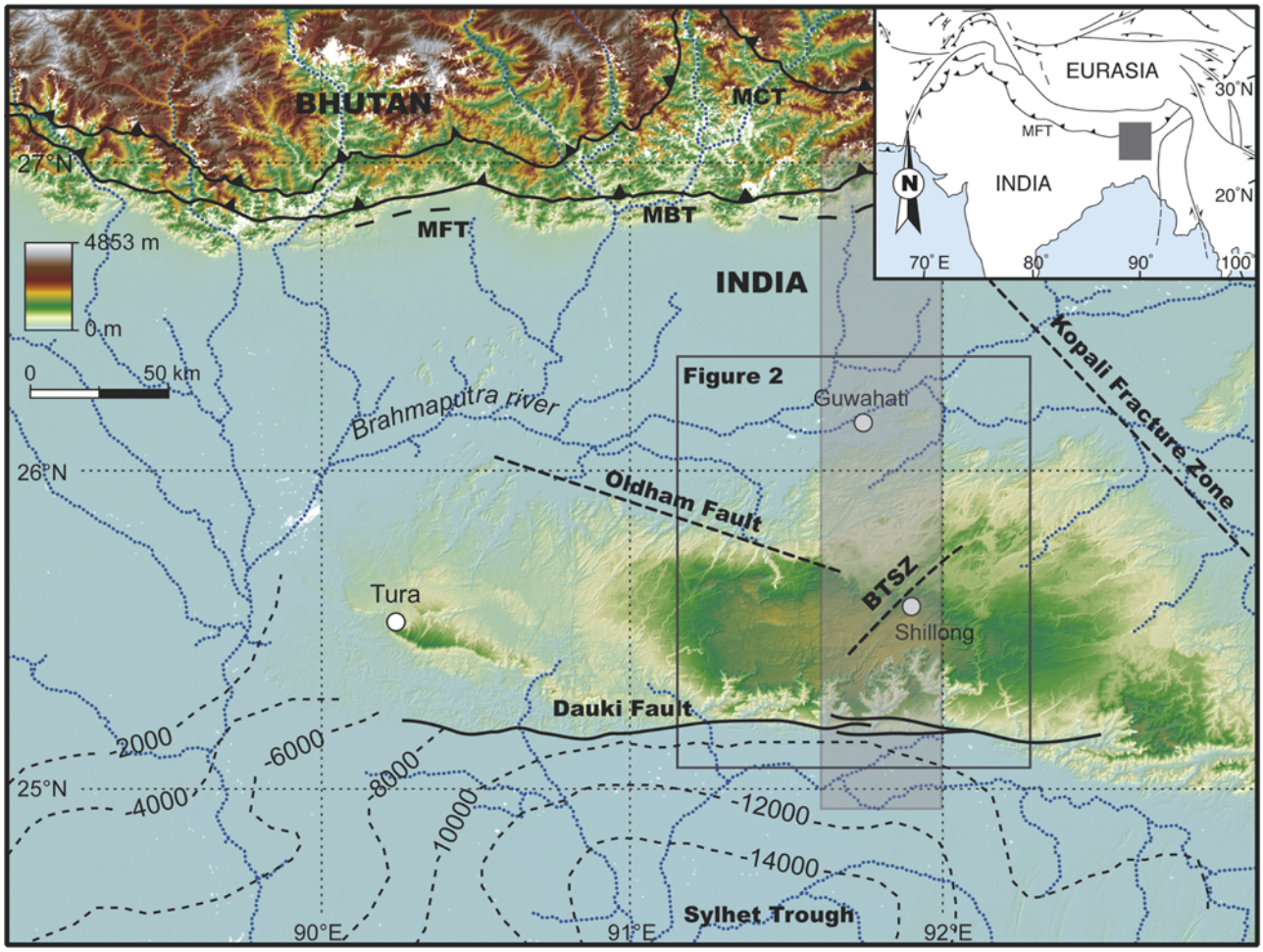

Figure 1. Digital topography and major structural features of southern Bhutan and Shillong plateau area. The heavy shaded box in inset shows the area covered by Figure 1. Topography is from SRTM 90 data (USGS). Structural data are from *Gansser* [1983] and *Biswas and Grasemann* [2005], sedimentary thickness in the Sylhet Trough is derived from *Shamsuddin and Abdullah* [1997] and is indicated in meters. BTSZ: Badapani-Tyrsad shear zone. Figure 2 covers the boxed area and the N-S elongated shaded box shows the location of the topographic swath profile shown in Figure 7a.

[*Bookhagen et al.*, 2005; *Grujic et al.*, 2006]. To constrain these couplings between climate-erosion-tectonics along the Himalayan range front, a fundamental step is to quantify (1) the timing and rate at which the Shillong plateau was uplifted, and (2) the partitioning of the India-Asia convergence into the Shillong plateau. To achieve this goal, thirteen samples located along a N-S trending transect across the Shillong plateau and collected at the top of it (Table 1) were analyzed using apatite and zircon (U-Th-[Sm])/He and apatite fission track analyses.

2. Geological Setting

[4] The Shillong plateau is considered to be a basement pop-up structure, uplifted along steep and seismically active reverse faults: the E-W trending Dauki fault in the south, and the inferred WNW-ESE trending Oldham Fault in the north [*Bilham and England*, 2001; *Biswas and Grasemann*,

Table 1. Sample Locations[a]

Sample Name	°N	°E	Elevation, m
GP5GN2	25.93472	91.87264	538
GP6GN3.3	25.91279	91.89176	582
GP6GN3.1	25.91275	91.89172	615
GP6GN3.2	25.91269	91.89166	594
GP6GN3	25.91265	91.89162	578
GP7S10	25.85077	91.88087	582
GP15/16	25.60434	91.55812	1700
GP15S13	25.59195	91.58945	1613
GP9S6	25.48945	91.82027	1696
GP13/14S10	25.40754	91.54295	1481
GP15S11	25.40337	91.52614	1464
GP11S8	25.37694	91.64790	1622
GP13GN9	25.37481	91.60673	1638

[a]GPS measurements were taken in the WGS 84 map datum.

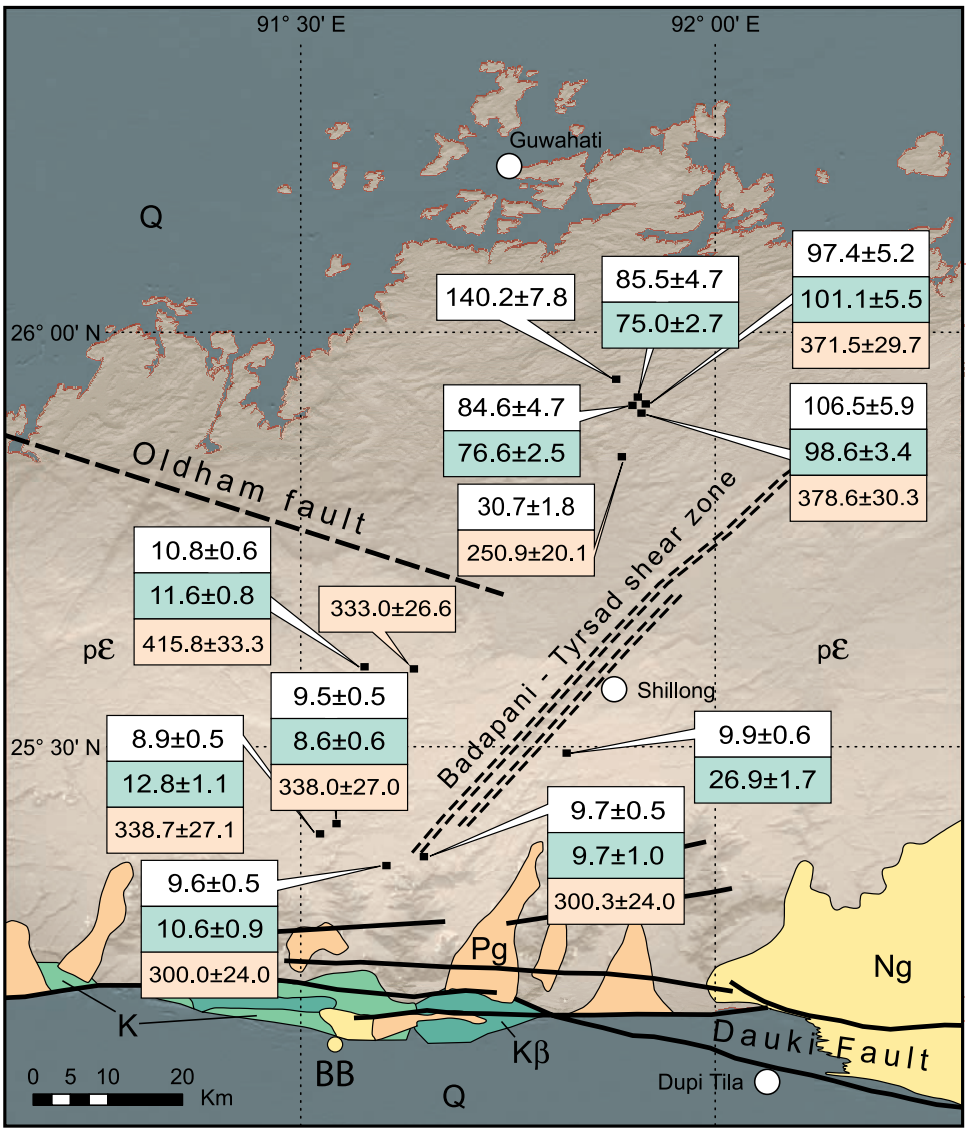

Figure 2. Topographic and geologic map of the central Shillong plateau (modified after *Sengupta et al.* [1998] and *Biswas and Grasemann* [2005]) showing the samples location. The apatite (U-Th-[Sm])/He ages are in white, apatite fission track ages are in green and zircon (U-Th)/He ages are in pink. Abbreviations and color coding are: Q, Quaternary deposits (heavy grey); Ng, Neogene deposits (yellow); Pg, Paleogene deposits (orange); K, Late Cretaceous continental sediments (light green); Kβ, Early Cretaceous intrusive and volcanic rocks (heavy green); pε, Protero-Paleozoic granitoids and metamorphic rocks (light brown); and BB, Boka Bil formation in the Chhatak drill hole [*Uddin and Lundberg*, 2004].

2005; *Kayal et al.*, 2006; *Rajendran et al.*, 2004] (Figures 1 and 2). The plateau is bounded by the Brahmaputra River to the west and by the NW-SE trending Kopali fracture zone in the east [*Acharyya et al.*, 1986; *Desikachar*, 1974; *Evans*, 1964; *Gupta and Sen*, 1988; *Nandy*, 1980]. The basement of the Shillong plateau is primarily composed of Precambrian metamorphic and intrusive rocks (Figure 2). Geochronological data from granitoids and pegmatites in Assam and Meghalaya yielded imprecise Rb-Sr whole-rock Neoproterozoic to Early Paleozoic ages between ~900 and ~450 Ma [*Ghosh et al.*, 1991; *Mitra and Mitra*, 2001; *Panneer Selvan et al.*, 1995; *van Breeman et al.*, 1989]. These rocks intrude Paleo-Mesoproterozoic gneisses [*Ghosh et al.*, 1994], which in the western Shillong plateau record prograde granulite facies anatexis at 1596 ± 15 Ma [*Chatterjee et al.*, 2007]. The initial exhumation of this Indian basement probably occurred during the late Paleozoic when a network of intracontinental sedimentary basins was established across Gondwana [*de Wit et al.*, 2001; *Veevers*, 2006; *Veevers and Tewari*, 1995]. Permo-Carboniferous continental sediments

are found in the coal basins near the town of Tura in the western part of Shillong plateau and to the west of Kolkata [*Veevers and Tewari*, 1995], but also at the base of the Lesser Himalaya Sequence in Bhutan to the north [*Gansser*, 1983]. Along the southern slopes of the Shillong plateau, small bodies of mafic igneous rocks, which are part of the Rajmahal-Sylhet flood basalt province, and ultramafic-alkaline-carbonatite complexes, are observed [*Das Gupta and Biswas*, 2000; *Srivastava et al.*, 2005] (Figure 2). On the basis of their geochemical signature, their structural position along N-S trending faults and their Early Cretaceous age, these rocks have been considered to be associated with the Kerguelen mantle plume [*Kent et al.*, 2002; *Ray et al.*, 2000; *Veena et al.*, 1988], which was active during the opening of the Indian Ocean between India and Australia-Antarctica [*Acharyya et al.*, 1980; *Alam*, 1989]. The onset of breakup between India and Antarctica is estimated to ~133 Ma and the initial massive pulse of Kerguelen magmatism and volcanism on top of the continental sediments and/or basement, occurred from ~120 to ~110 Ma [*Coffin et al.*, 2002].

[5] The presence of Late Cretaceous continental sediments lying unconformably on the Precambrian bedrock in the southern part of the plateau indicates that the basement was exposed at the surface at the end of the Cretaceous. However, during the Tertiary the basement was submerged and buried under shallow marine and deltaic sediments; that is, it acted as the passive margin of the Indian plate. The thickest preserved section reaches ~3000 m in the SW part of the plateau [*Chakraborty*, 1972]. In our study area (Figure 2), the southern fringe of the plateau displays a ~1000-m-thick sedimentary cover of Cretaceous-Tertiary deposits [*Jauhri and Agarwal*, 2001] on a gently (5°–10°) south-dipping, roughly flat basement. The basal member of this sequence, the Khasi formation (70.6–65.5 Ma, Maastrichtian), comprises channel-filled and floodplain facies [*Mamallan et al.*, 1995; *Mishra and Sen*, 2001]. Burial by marine sedimentation started at the end of the Maastrichtian Stage at ~65–66 Ma [*Mishra and Sen*, 2001]. A carbonate platform persisted until the late Middle-Late Eocene when a terrigenous influx initiated deposition of thick clastic sequences during the late Paleogene and Neogene in the southern part of the plateau [*Jauhri and Agarwal*, 2001]. The mainly fine-grained pro-delta sediments of the Surma Group, deposited during the Miocene and the Early Pliocene, are interpreted as recording increased exhumation and erosion of Himalayan rocks [*Johnson and Alam*, 1991; *Najman*, 2006; *Uddin and Lundberg*, 2004], while the southern part of the Shillong plateau and the Sylhet Trough remained submerged [*Johnson and Alam*, 1991]. An abrupt facies change at ~3.8–3.5 Ma to coarse-grained braided-fluvial sandstones of the Tipam formation marks the transition from marine to continental sedimentation in the Sylhet Trough [*Najman*, 2006].

[6] The timing of the surface uplift of the Shillong plateau remains poorly constrained and in the literature, is often confused with the timing of its exhumation. Namely, for a basement outcrop, the rates of rock uplift, rock exhumation and surface uplift are not necessarily the same and their onset does not need to be coeval. On the basis of relatively homogeneous thicknesses of Miocene strata in the Sylhet Trough, significant displacement along the Dauki fault is thought to have started only after the Miocene [*Uddin and Lundberg*, 2004]. Lithofacies and depositional environment changes indicate that the southern foothills of the Shillong plateau were submerged until 3.8–3.5 Ma [*Worm et al.*, 1998]. The Shillong plateau emerged as an outcrop of Precambrian basement rocks sometimes in the late Pliocene as corroborated by lithofacies trends suggesting that the Shillong basement was not a source of sediments during the Miocene [*Johnson and Alam*, 1991; *Uddin and Lundberg*, 1999]. The lack of deposition on the Shillong plateau in the Pliocene supports the interpretation of an emerging plateau [*Johnson and Alam*, 1991]. Uplift of the plateau led to a reorganization of the rivers. Sedimentary data suggest that the paleo-Brahmaputra flowed to the south of the plateau until the Miocene [*Uddin and Lundberg*, 1999], and was deflected in the Pliocene, 300 km west and northward to its present course behind the plateau [*Uddin and Lundberg*, 1999].

3. Apatite and Zircon (U-Th-[Sm])/He Dating

3.1. Methodology

[7] Apatite (U-Th-[Sm])/He dating is a well-established thermochronometric technique that is widely employed in geological, tectonic, and geomorphologic studies [e.g., *Ehlers and Farley*, 2003; *Farley and Stockli*, 2002; *Stockli*, 2005; *Stockli et al.*, 2000]. (U-Th-[Sm])/He dating is based on the decay of ^{235}U, ^{238}U, ^{232}Th, and ^{147}Sm by alpha (^{4}He nucleus) emission. The decay energy, up to ~8 MeV, is taken up mostly in the form of α-recoil of the parent nucleus and energetic emission of the α particle [*Farley et al.*, 1996]. Alpha particles are emitted with high kinetic energy and travel significant distances before coming to rest, leading to potential α loss from the grain during decay. Thus measured (U-Th)/He ages are reduced by this ejection effect; an ejection effect that is commonly and viably corrected for using a statistical approach taking into account mineral density and crystal geometry [*Farley*, 2002; *Farley et al.*, 1996; *Meesters and Dunai*, 2002]. The ^{4}He is completely lost by thermally activated diffusion from apatite at temperatures above ~80°C and quantitatively retained below ~40°C (termed the He Partial Retention Zone, HePRZ) [e.g., *Stockli et al.*, 2000; *Wolf et al.*, 1998]. Assuming a mean annual surface temperature of 10 ± 5°C and a geothermal gradient of 25°C/km, the relevant temperature range is equivalent to depths of ~1 to 3 km.

[8] Several physical parameters have been shown to affect He diffusivity in apatite. He diffusivity appears to positively correlate with the physical dimensions of the apatite crystal, so grain size has a small effect on the closure temperature [*Farley*, 2002; *Reiners and Farley*, 2001]. More recently, Shuster and others [*Shuster et al.*, 2006] have demonstrated the effect of α-recoil radiation damage on He retentivity in apatite and demonstrated that He retentivity

Table 2. Apatite (U-Th-[Sm])/He Data From the Shillong Plateau[a]

Sample	Age, Ma	Error (2σ), Ma	U, ppm	Th, ppm	Sm, ppm	eU, ppm	Th/U	He, ncc/mg	Mass, μg	Ft
					Group 1					
GP6GN3-1	101.6	5.1	28.8	101.4	115.2	52.6	3.521	517.9	12.6	0.78
GP6GN3-2	98.0	4.9	16.7	56.8	90.6	30.1	3.393	267.0	7.1	0.72
GP6GN3-3	109.6	5.5	19.2	76.5	97.3	37.2	3.988	350.5	5.0	0.69
GP6GN3-10[b]	237.0	14.2	23.3	88.7	72.6	44.2	3.797	825.0	3.8	0.63
GP6GN3-11	116.0	7.0	29.8	120.8	78.0	58.2	4.050	507.0	3.2	0.61
GP6GN3-12[b]	136.1	8.2	29.6	125.6	71.6	59.1	4.245	710.5	4.1	0.71
GP6GN3-13	110.4	6.6	51.6	206.9	83.3	100.2	4.010	930.4	3.1	0.68
GP6GN3-14	103.5	6.2	26.1	104.8	100.2	50.7	4.021	435.9	2.9	0.67
GP6GN3	***106.5***	***5.9***	***28.7***	***111.2***	***94.1***	***54.8***	***3.830***	***501.4***	***5.7***	***0.69***
GP6GN3.1-1[b]	290.7	14.5	19.3	36.1	43.6	27.7	1.872	703.8	6.0	0.71
GP6GN3.1-3	104.9	5.2	15.9	31.6	68.7	23.3	1.994	229.2	10.5	0.77
GP6GN3.1-4	100.9	5.0	25.6	51.8	56.7	37.7	2.026	350.1	2.9	0.75
GP6GN3.1-5	100.4	5.0	37.6	75.5	34.6	55.3	2.006	500.6	2.5	0.74
GP6GN3.1-6	99.3	4.6	15.6	36.8	95.3	24.2	2.362	213.0	5.1	0.79
GP6GN3.1-12	96.6	5.8	25.9	84.9	137.2	45.8	3.276	382.3	3.3	0.69
GP6GN3.1-13	93.0	5.6	18.0	59.4	66.1	32.0	3.294	268.2	9.6	0.72
GP6GN3.1-14[b]	210.1	12.6	28.6	96.3	99.8	51.3	3.362	900.3	5.2	0.67
GP6GN3.1-15	86.8	5.2	31.0	118.3	165.6	58.8	3.821	453.4	4.0	0.71
GP6GN3.1	***97.4***	***5.2***	***24.2***	***65.5***	***89.2***	***39.6***	***2.683***	***342.4***	***5.4***	***0.74***
GP6GN3.2-1	82.6	4.1	23.7	37.5	45.8	32.5	1.582	237.4	6.1	0.72
GP6GN3.2-2[b]	113.8	5.7	15.9	25.1	47.7	21.8	1.582	232.1	9.1	0.75
GP6GN3.2-3	99.9	5.0	17.3	41.8	64.3	27.1	2.422	245.7	6.2	0.73
GP6GN3.2-9	78.0	4.7	14.6	33.0	58.4	22.4	2.253	155.4	7.7	0.71
GP6GN3.2-10	79.8	4.8	33.1	70.5	101.0	49.7	2.128	334.8	5.0	0.68
GP6GN3.2-11	82.5	4.9	20.6	49.7	57.5	32.2	2.417	212.6	3.8	0.64
GP6GN3.2-12[b]	15.3	0.9	24.8	55.5	72.6	37.8	2.238	46.0	3.4	0.64
GP6GN3.2	***84.6***	***4.7***	***21.9***	***46.5***	***65.4***	***32.8***	***2.160***	***237.2***	***5.8***	***0.70***
GP6GN3.3-1[b]	231.8	11.6	28.7	100.3	59.5	52.3	3.491	1056.2	5.3	0.70
GP6GN3.3-2[b]	161.2	8.1	26.1	87.2	97.6	46.6	3.340	658.9	5.5	0.70
GP6GN3.3-3[b]	305.9	15.3	12.6	25.6	131.2	18.6	2.037	548.5	7.7	0.74
GP6GN3.3-4	104.8	5.2	16.6	61.7	45.7	31.1	3.706	264.7	1.1	0.66
GP6GN3.3-5	105.5	5.3	18.2	78.5	75.7	36.7	4.312	310.0	1.4	0.66
GP6GN3.3-6[b]	127.6	6.4	16.7	60.1	85.6	30.8	3.597	332.1	1.4	0.69
GP6GN3.3-12	73.1	4.4	16.0	47.3	64.2	27.1	2.961	148.9	2.8	0.60
GP6GN3.3-13	60.7	3.6	18.7	43.1	69.7	28.8	2.306	145.0	4.6	0.67
GP6GN3.3-14	83.5	5.0	25.3	52.4	70.9	37.6	2.074	242.9	3.0	0.62
GP6GN3.3	***85.5***	***4.7***	***19.0***	***56.6***	***65.2***	***32.3***	***3.072***	***222.3***	***2.6***	***0.64***
GP5GN2-1	132.3	6.6	37.9	115.3	114.8	65.0	3.045	741.2	5.3	0.69
GP5GN2-2	146.4	7.3	38.4	137.0	204.0	70.6	3.566	882.8	4.5	0.68
GP5GN2-3	144.5	7.2	48.6	155.8	163.6	85.2	3.203	1049.0	4.8	0.68
GP5GN2-9	153.3	9.2	51.2	155.4	122.8	87.7	3.033	1043.6	3.2	0.63
GP5GN2-10	113.7	6.8	40.5	133.6	158.9	71.9	3.296	672.0	4.9	0.66
GP5GN2-11	165.5	9.9	41.3	122.7	206.3	70.1	2.974	1038.0	4.5	0.71
GP5GN2-12	125.6	7.5	36.8	104.8	176.0	61.5	2.847	674.9	3.9	0.70
GP5GN2	***140.2***	***7.8***	***42.1***	***132.1***	***163.8***	***73.1***	***3.138***	***871.6***	***4.4***	***0.68***
GP7S10-1	25.6	1.5	8.5	42.5	168.8	18.5	4.997	40.1	2.2	0.65
GP7S10-2	35.9	2.2	17.3	104.7	269.4	41.9	6.061	121.4	1.7	0.63
GP7S10-3[b]	52.9	3.2	22.4	136.9	328.2	54.6	6.110	232.6	1.8	0.63
GP7S10	***30.7***	***1.8***	***12.9***	***73.6***	***219.1***	***30.2***	***5.529***	***80.7***	***2.0***	***0.64***
					Group 2					
GP9S6-1[b]	60.1	3.0	22.1	80.5	200.3	41.0	3.643	239.1	10.1	0.75
GP9S6-2[b]	24.3	1.2	22.4	97.2	1064.5	45.2	4.344	104.2	3.2	0.65
GP9S6-3	9.9	0.5	16.2	81.7	877.5	35.4	5.050	33.3	3.2	0.65
GP9S6-4[b]	26.7	1.3	15.0	48.7	210.5	26.4	3.255	59.0	1.3	0.69
GP9S6-5[b]	30.3	1.5	14.4	45.0	531.5	25.0	3.127	59.3	1.2	0.64
GP9S6-6	10.0	0.6	7.1	35.6	690.7	15.5	5.021	15.7	1.0	0.64
GP9S6	***9.9***	***0.6***	***11.6***	***58.7***	***784.1***	***25.4***	***5.036***	***24.5***	***2.1***	***0.65***
GP11S8-1[b]	13.6	0.7	43.2	211.6	841.7	93.0	4.895	103.6	1.7	0.63
GP11S8-2	9.7	0.5	11.3	80.9	410.0	30.3	7.173	27.9	1.9	0.64
GP11S8-3	10.7	0.5	23.7	80.8	602.8	42.7	3.415	62.4	4.8	0.73
GP11S8-4[b]	14.8	0.7	59.1	286.0	567.0	126.3	4.841	142.7	1.1	0.63
GP11S8-5	8.5	0.4	52.0	222.6	493.5	104.3	4.279	74.1	2.5	0.71
GP11S8-6	9.7	0.6	12.1	47.3	593.4	23.2	3.900	19.4	1.0	0.62
GP11S8	***9.7***	***0.5***	***24.8***	***107.9***	***524.9***	***50.1***	***4.692***	***45.9***	***2.6***	***0.67***
GP13/14S10-1	9.5	0.5	23.1	69.5	89.8	39.5	3.001	38.5	9.2	0.75
GP13/14S10-2[b]	14.5	0.7	56.0	196.0	164.8	102.1	3.498	126.5	3.7	0.69
GP13/14S10-3[b]	17.7	0.9	35.6	125.3	118.9	65.1	3.519	97.0	2.9	0.68

Table 2. (continued)

Sample	Age, Ma	Error (2σ), Ma	U, ppm	Th, ppm	Sm, ppm	eU, ppm	Th/U	He, ncc/mg	Mass, μg	Ft
GP13/14S10-4	9.8	0.5	30.9	108.0	87.6	56.3	3.496	48.2	1.2	0.65
GP13/14S10-5	9.2	0.5	11.2	26.2	114.5	17.3	2.344	16.8	4.5	0.79
GP13/14S10	***9.5***	***0.5***	***21.7***	***67.9***	***97.3***	***37.7***	***2.947***	***34.5***	***5.0***	***0.73***
GP13GN9-1	9.8	0.5	38.8	146.2	4929.2	73.1	3.774	97.4	4.3	0.72
GP13GN9-2	8.8	0.4	64.2	224.5	2204.6	117.0	3.496	150.3	5.4	0.66
GP13GN9-3	10.3	0.5	11.4	33.5	1434.7	19.3	2.943	22.7	6.0	0.73
GP13GN9-10	8.1	0.5	38.9	145.6	597.1	73.1	3.744	52.0	6.0	0.67
GP13GN9-11	8.9	0.5	39.8	146.1	722.2	74.1	3.673	57.1	4.5	0.66
GP13GN9-12	11.1	0.7	35.3	128.6	498.5	65.5	3.647	74.2	5.3	0.73
GP13GN9-13	10.5	0.6	15.3	43.8	292.3	25.6	2.862	25.1	3.8	0.70
GP13GN9	***9.6***	***0.5***	***34.8***	***124.1***	***1525.5***	***64.0***	***3.448***	***68.4***	***5.0***	***0.70***
GP15/16-1	11.5	0.6	84.3	194.4	650.5	130.0	2.307	139.4	3.4	0.68
GP15/16-2	10.4	0.5	102.3	311.3	1629.9	175.5	3.043	242.0	3.4	0.67
GP15/16-3 [b]	18.2	0.9	117.0	344.0	545.5	197.8	2.941	306.8	4.9	0.70
GP15/16-4[b]	23.7	1.1	159.7	492.0	151.0	275.3	3.081	535.7	1.8	0.70
GP15/16-5	9.7	0.6	83.2	169.3	241.8	123.0	2.035	124.2	1.2	0.65
GP15/16-6	9.9	0.5	241.1	1046.0	367.2	486.9	4.338	440.4	1.4	0.68
GP15/16-12	11.6	0.7	218.7	517.3	1045.8	340.2	2.366	338.9	2.1	0.58
GP15/16-13[b]	22.3	1.3	205.2	548.8	1020.0	334.2	2.674	566.1	3.1	0.61
GP15/16-14	11.3	0.7	146.4	427.2	791.2	246.8	2.917	211.6	2.9	0.60
GP15/16-15	10.8	0.7	121.8	410.6	764.9	218.3	3.372	225.3	2.0	0.64
GP15/16	***10.8***	***0.6***	***142.5***	***439.5***	***784.5***	***245.8***	***2.911***	***246.0***	***2.3***	***0.64***
GP15S11-1	9.8	0.5	35.5	179.6	1106.8	77.7	5.062	68.6	3.2	0.66
GP15S11-2	9.3	0.5	53.3	379.5	2477.9	142.5	7.124	120.2	3.1	0.65
GP15S11-3	8.5	0.4	31.5	191.4	772.6	76.5	6.080	78.3	6.1	0.75
GP15S11-9	8.7	0.5	29.0	181.7	796.6	71.7	6.261	44.3	1.6	0.53
GP15S11-10[b]	16.3	1.0	55.4	357.2	676.7	139.3	6.452	181.6	2.0	0.63
GP15S11-11	7.8	0.5	43.9	256.1	901.9	104.1	5.834	69.2	2.5	0.66
GP15S11-12	9.5	0.6	46.5	358.0	1027.0	130.7	7.691	96.8	1.6	0.60
GP15S11	***8.9***	***0.5***	***40.0***	***257.7***	***1180.5***	***100.5***	***6.342***	***79.5***	***3.0***	***0.64***

[a]Single grain laser apatite (U-Th-[Sm])/He age determinations were carried out at the University of Kansas laboratory using laboratory procedures as described by *Stockli et al.* [2000] and *House et al.* [2001]. Inclusion-free apatite grains were wrapped in acid-treated Pt foil and heated for 5 min at 1070°C and subsequently reheated to ensure complete degassing. After laser heating, apatites were spiked using an enriched $^{235}U^{-230}Th^{-149}Sm$ tracer and dissolved in HNO_3. U, Th, and Sm concentrations were determined by isotope dilution ICP-MS analysis. Here eU is the effective uranium concentration (where eU = U + 0.235Th) [*Shuster et al.*, 2006]. Ft factor refers to α-ejection correction factor [*Farley et al.*, 1996].

[b]Analyses were not taken in account when calculating the mean values.

correlates with total radiation damage. Increased He retentivity due to the accumulation of radiation damage demonstrably results in a significant increase in effective closure temperature (T_{ec}) over long radiation damage accumulation times. This relationship is readily observable in the correlation of (U-Th)/He ages with the effective uranium concentration eU (where eU = U + 0.235Th). The annealing kinetics of radiation damage in apatite is not yet fully understood, but Shuster and others [*Shuster et al.*, 2006] suggest that heating to temperatures >150°C removes radiation damage. This effective increase in He retentivity, therefore, dramatically affects samples that reside at temperatures <150°C during protracted cooling or moderate reheating during burial [*Flowers et al.*, 2006] (also this study). Radiogenic He concentrations can be used as proxy for radiation damage; however, He concentration only represents a minimum measure of radiation damage, since He can be partially or completely lost well below radiation damage annealing temperatures.

[9] In many minerals, such as zircon, the contribution of ^{4}He from ^{147}Sm is minor or negligible compared to that from U and Th, owing to low concentrations of Sm, the significantly lower decay constant, and the fact that Sm contributes only one α particle. However, apatite can contain considerable amounts of Sm that significantly affect measured (U-Th)/He ages. In this study, some of the analyzed apatites were characterized by unusually high Sm concentrations (Table 2), lowering calculated (U-Th)/He ages by as much as 9%. All reported ages in this study were calculated incorporating the ^{147}Sm contribution.

[10] More recently, other U- and Th-bearing minerals, such as titanite, zircon, and monazite have attracted interest as potential geo- and thermo-chronometers [e.g., *Boyce et al.*, 2006; *Farley and Stockli*, 2002; *Reiners*, 2005; *Reiners and Farley*, 1999; *Reiners et al.*, 2002, 2004; *Stockli and Farley*, 2004]. Each of these mineral phases is characterized by distinct He diffusion kinetics and closure temperatures. The most commonly used (U-Th)/He thermochronometer besides apatite, is zircon, which is characterized by a He closure temperature ranging from ~180°–200°C [e.g., *Reiners et al.*, 2004] and a HePRZ spanning a temperature range from ~120° to 180°C [*Stockli*, 2005; *Tagami et al.*, 2003]. So far, no quantitative measure of the He retentivity as a function of accumulated radiation damage exists, analogous to apatite [*Shuster et al.*, 2006]). However, it is well known that He diffusion in zircon is strongly affected at relatively high degrees of radiation damage, leading to a lowering in He retentivity [e.g., *Reiners*, 2005, and refer-

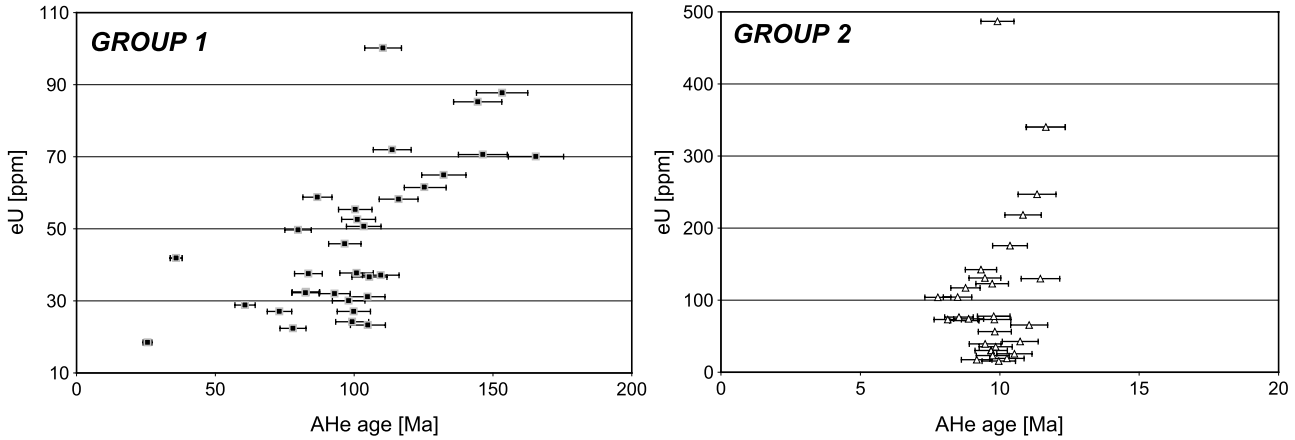

Figure 3. Apatite (U-Th-[Sm])/He ages versus effective uranium concentration eU. Group 1 apatite analyses show a remarkably clear trend of increasing (U-Th-[Sm])/He ages with increasing eU, suggesting the expected correlation of He retentivity with radiation damage [*Shuster et al.*, 2006].

ences therein]. The effects of radiation damage on He diffusivity have been shown to become important at radiation dosages >2–4 $\times$ 10^{18} α/g levels at which signs of metamictization are readily observable [*Nasdala et al.*, 2004; *Reiners*, 2005; *Reiners et al.*, 2004].

[11] (U-Th-[Sm])/He age determinations were carried out at the University of Kansas using laboratory procedures described by *Stockli et al.* [2000] and *House et al.* [2001]. All ages were calculated using standard α-ejection corrections using morphometric analyses [*Farley*, 2002; *Farley et al.*, 1996]. Mean (U-Th-[Sm])/He ages were calculated on the basis of 2–9 inclusion-free apatite and 3–4 zircon replicate analyses. Reported age uncertainties (2-σ) reflect the reproducibility of replicate analyses of laboratory standard samples [*Farley et al.*, 2001]. Estimated analytical uncertainties are ~6% (2-σ) for apatite and ~8% (2-σ) for zircon He ages, respectively.

3.2. Results

3.2.1. Apatite (U-Th-[Sm])/He Results

[12] Shillong apatite samples are very radiogenic (11–150 ppm U and 47–461 ppm Th) and more importantly also vary significantly in Sm content (64–1180 ppm). Unusually high Sm concentrations in some samples (e.g., GP13GN9 and GP15S11) result in significant contribution to He ingrowth and age. It is also noteworthy that parent nuclide concentrations not only vary from sample to sample, but exhibit surprisingly large variations from replicate to replicate analysis of individual samples. For example sample GP15/16 is characterized by a eU of 253 ± 111 ppm (~44% RSD).

[13] Samples from the northern portion of the Shillong plateau (Group 1) yield middle to late Cretaceous apatite (U-Th-[Sm])/He ages. All but one, are within error identical to the apatite fission track ages (Table 2 and Figure 2). Individual replicate analyses scatter considerably more about the mean than commonly observed in laboratory standard samples, with some replicate ages exceeding apatite fission track ages. Given the apparent ages and high parent nuclide concentrations of Group 1 apatite, the He retentivity should be significantly impacted by the accumulation of radiation damage. Group 1 apatite analyses show a remarkably clear trend of increasing (U-Th-[Sm])/He ages with increasing eU, suggesting the expected correlation of He retentivity with radiation damage (Figure 3). On the basis of the relationship between the He concentration and the effective closure temperature (T_{ec}) given by *Shuster et al.* [2006], estimated T_{ec} values range from ~57° to 87°C. These values are minimum estimates due to potential loss of He at temperatures below the limit of radiation damage annealing. This observed age versus eU relationship indicates that burial by Tertiary sediments was limited. The similarity of apatite fission track and (U-Th-[Sm])/He ages, despite the protracted thermal history, suggests that increased He retentivity due to radiation damage results in effective He closure temperatures for high eU apatite that approach the closure temperature of the apatite fission track system.

[14] Apatite (U-Th-[Sm])/He ages of samples from top and the southern margin of the plateau, in the hanging wall of the Dauki fault (Group 2), are all Miocene in age (Table 2). These younger apatite (U-Th-[Sm])/He ages are within error equal or slightly younger than the corresponding apatite fission track ages (Figure 2). In contrast to samples from the northern Shillong plateau, Group 1 apatite samples are characterized by substantially higher parent nuclide concentrations (up to 5 times higher eU). However, those samples show no significant age difference and no age correlation with eU, suggesting that accumulated radiation damage was completely annealed prior to Late Miocene exhumation (Figure 3). According to *Shuster et al.* [2006], the critical temperature above which the effect of radiation damage becomes negligible is ~90°C, based on their thermal model parameters. This appears to be in good agreement with our results given the lack of correlation between (U-Th-[Sm])/He ages and eU for samples with completely reset apatite fission track ages (T $\geq$ 110°C). Thus these results

Table 3. Zircon (U-Th)/He Data From the Shillong Plateau[a]

Sample	Age, Ma	Error (2σ), Ma	U, ppm	Th, ppm	α-dose, α/g	Th/U	He, ncc/mg	Mass, μg	Ft
				Group 1					
GP6GN3-1	382.9	30.6	217.6	126.5	3.33E + 16	0.58	9314.4	7.6	0.78
GP6GN3-2	347.9	27.8	186.2	283.6	3.40E + 16	1.52	8295.0	4.7	0.76
GP6GN3-3	360.3	28.8	537.6	590.4	9.10E + 16	1.10	23020.2	4.7	0.76
GP6GN3-4	423.2	33.9	324.4	416.7	5.68E + 16	1.28	16683.5	4.9	0.74
GP6GN3	***378.6***	***30.3***	***316.4***	***354.3***	***5.38E + 16***	***1.12***	***14328.3***	***5.5***	***0.76***
GP6GN3.1-1	379.2	30.3	416.3	205.6	6.26E + 16	0.49	16470.5	4.7	0.75
GP6GN3.1-2	354.6	28.4	280.5	222.6	4.48E + 16	0.79	10730.6	3.9	0.73
GP6GN3.1-3	380.5	30.4	326.4	258.9	5.21E + 16	0.79	13722.7	4.8	0.74
GP6GN3.1	***371.5***	***29.7***	***341.1***	***229.0***	***5.32E + 16***	***0.69***	***13641.3***	***4.5***	***0.74***
GP7S10-1	267.5	21.4	403.1	272.2	6.29E + 16	0.68	11690.6	4.8	0.75
GP7S10-2	244.2	19.5	416.3	285.8	6.51E + 16	0.69	10547.3	3.2	0.72
GP7S10-3	241.2	19.3	393.0	192.2	5.90E + 16	0.49	9803.4	5.0	0.75
GP7S10	***250.9***	***20.1***	***404.2***	***250.1***	***6.24E + 16***	***0.62***	***10680.4***	***4.3***	***0.74***
				Group 2					
GP11S8-1	268.3	21.5	140.9	100.3	2.22E + 16	0.71	4238.0	6.3	0.77
GP11S8-2	329.8	26.4	201.8	145.0	3.18E + 16	0.72	7670.8	9.1	0.79
GP11S8-3	302.8	24.2	239.7	146.4	3.69E + 16	0.61	7869.4	5.7	0.76
GP11S8	***300.3***	***24.0***	***194.1***	***130.6***	***3.03E + 16***	***0.68***	***6592.7***	***7.0***	***0.77***
GP13/14S10-1	329.5	26.4	154.7	170.7	2.62E + 16	1.10	5767.5	3.5	0.72
GP13/14S10-2	355.6	28.4	252.8	164.7	3.93E + 16	0.65	9408.2	4.0	0.73
GP13/14S10-3	328.8	26.3	173.8	122.0	2.73E + 16	0.70	6295.7	5.2	0.76
GP13/14S10	***338.0***	***27.0***	***193.8***	***152.5***	***3.09E + 16***	***0.82***	***7157.2***	***4.2***	***0.74***
GP13GN9-1	272.0	21.8	184.3	96.3	2.79E + 16	0.52	5497.2	7.4	0.79
GP13GN9-2	335.2	26.8	163.6	122.1	2.59E + 16	0.75	6298.4	7.3	0.78
GP13GN9-3	292.8	23.4	231.5	154.2	3.61E + 16	0.67	7724.2	8.4	0.79
GP13GN9	***300.0***	***24.0***	***193.1***	***124.2***	***2.99E + 16***	***0.64***	***6506.6***	***7.7***	***0.79***
GP15/16-1	363.4	29.1	125.0	118.7	2.06E + 16	0.95	4952.2	3.5	0.71
GP15/16-2	421.2	33.7	97.2	94.3	1.61E + 16	0.97	4583.6	4.1	0.73
GP15/16-3	463.0	37.0	40.4	45.0	6.86E + 15	1.11	2273.1	6.2	0.76
GP15/16	***415.8***	***33.3***	***87.5***	***86.0***	***1.45E + 16***	***1.01***	***3936.3***	***4.6***	***0.74***
GP15S11-1	339.2	27.1	179.1	186.6	3.00E + 16	1.04	6692.7	3.3	0.71
GP15S11-2	376.7	30.1	357.3	267.0	5.66E + 16	0.75	14601.0	4.9	0.74
GP15S11-3	300.3	24.0	334.5	247.1	5.29E + 16	0.74	10737.2	5.1	0.73
GP15S11	***338.7***	***27.1***	***290.3***	***233.6***	***4.65E + 16***	***0.84***	***10677.0***	***4.4***	***0.73***
GP15S13-1	311.3	24.9	154.9	49.0	2.24E + 16	0.32	4898.8	4.6	0.76
GP15S13-2	332.9	26.6	191.9	72.9	2.82E + 16	0.38	6392.2	3.9	0.74
GP15S13-3	354.8	28.4	204.4	67.6	2.97E+16	0.33	7392.3	4.9	0.76
GP15S13	***333.0***	***26.6***	***183.7***	***63.2***	***2.68E + 16***	***0.34***	***6227.8***	***4.5***	***0.75***

[a]Inclusion-free zircons were wrapped in Pt foil, heated for 10 min at 1290°C, and reheated until >99% of the He was extracted from the crystal. All ages were calculated using standard α-ejection corrections using morphometric analyses [*Farley*, 2002; *Farley et al.*, 1996]. Zircons were unwrapped from Pt foil and dissolved using HF-HNO3 and HCl pressure vessel digestion procedures. U and Th concentrations were determined by isotope dilution ICP-MS analysis. Here α-dose is the radiation dosage calculated for the present U and Th content and age. Ft factor refers to α-ejection correction factor [*Farley et al.*, 1996].

from Group 2 apatite suggest rapid middle to late Miocene cooling from temperatures significantly >90°C.

3.2.2. Zircon (U-Th)/He Results

[15] All zircon (U-Th)/He ages range from ~250 to 350 Ma and show no correlation with the age groups defined by the apatite results (Table 3). While individual zircon samples are characterized by internally reproducible analyses (three to four replicates), different samples exhibit considerable age difference. This spread is likely attributable to long residence in the zircon HePRZ and very slow exhumation rates, possibly amplifying any kinetic or zonation effects on apparent ages [e.g., *Hourigan et al.*, 2005; *Reich et al.*, 2007]. In order to assess potential He loss due to high degrees of radiation damage (metamictization), we estimated total α-dosage values, assuming recoil damage accumulation since 400 Ma (maximum apparent zircon (U-Th)/He age), using the equation of *Nasdala et al.* [2004]. Total α-dosages for all zircons range from $\sim 7 \times 10^{15}$ to 9×10^{16} and do not exceed the critical value of $\sim 3.5 \times 10^{18}$ α-events/g given by *Nasdala et al.* [2004]. This suggests that He loss related to radiation damage has likely played a negligible role. These zircon (U-Th)/He data imply that rocks exposed in the Shillong plateau have resided in an upper crustal position at least since early Paleozoic times (<8 km assuming a geothermal gradient of 25°C/km and nominal Tc).

4. Apatite Fission Track Thermochronology

4.1. Methodology

[16] Fission track thermochronology is based on the spontaneous fission decay of ^{238}U in uranium-bearing

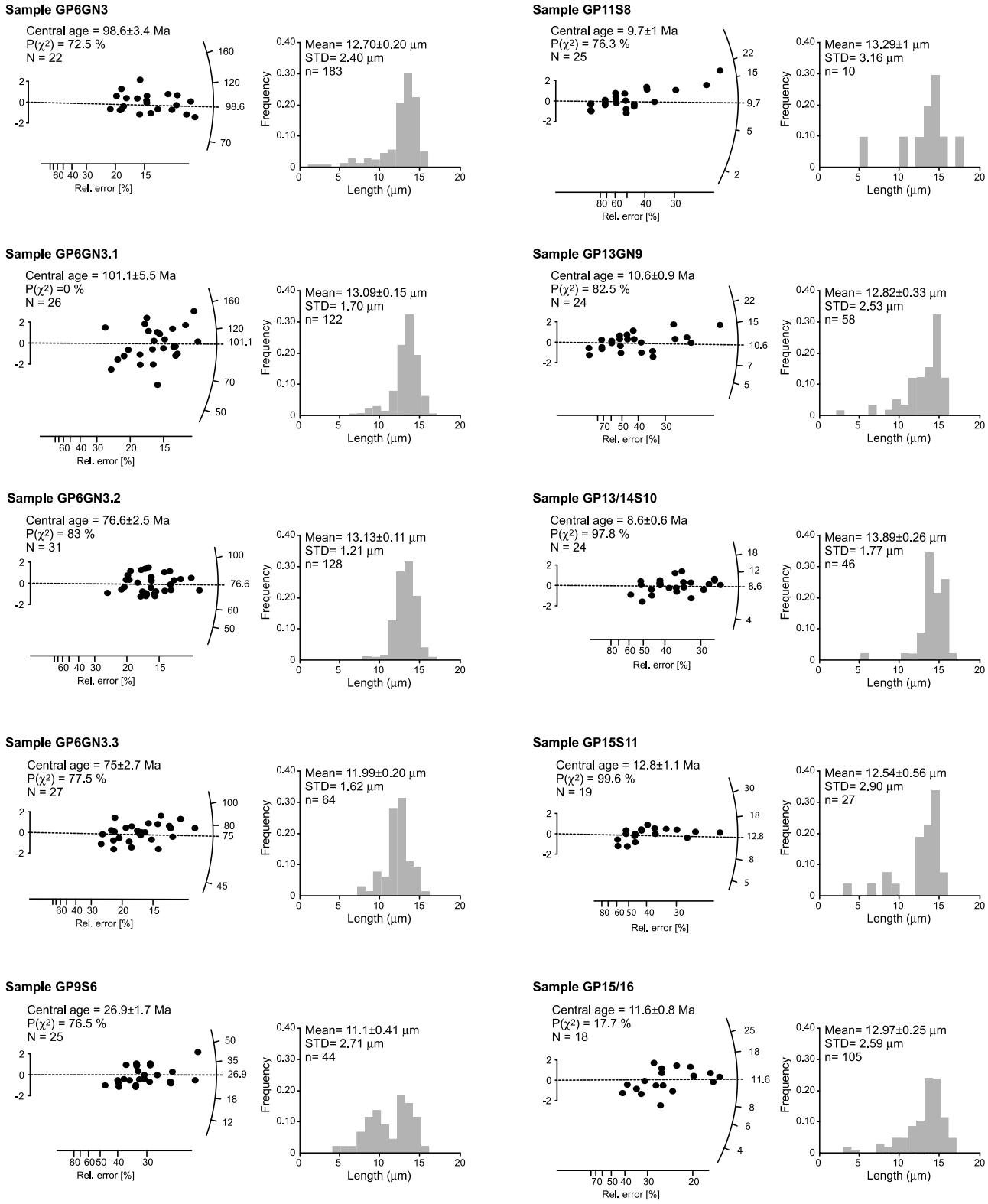

Figure 4. Apatite fission track results: radial plots of the single-grain age data, and track length histograms; N, number of individual grains dated per sample; P(χ^2), chi-square probability; n, number of individual track measured. Mean track lengths are not *c*-axis corrected. Trackkey software [*Dunkl*, 2002] was used for calculating the central fission track ages $\pm 1\sigma$.

Table 4. Apatite Fission Track Data From the Shillong Plateau[a]

Sample	Number of Grains (N)	Spontaneous Track Density, $\rho s \times 10^5$ cm^{-2} (Ns)	Induced Track Density, $\rho i \times 10^5$ cm^{-2} (Ni)	Dosimeter, $\rho d \times 10^5$ cm^{-2} (Nd)	P(χ^2), %	Central Age ± 1σ, Ma	U, ppm	Number of Confined TL	MTL (Not Corrected), μm ± 1σ	MTL STD, μm	MTL (c-Axis Corrected), μm ± 1σ	Number of Dpars	Dpars, μm	Dpars STD, μm
GP6GN3.3	27	7.571 (1388)	19.888 (3646)	10.708 (8736)	77.5	75 ± 2.7	21.5	64	11.99 ± 0.20	1.62	14.04 ± 0.99	128	1.85 ± 0.01	0.14
GP6GN3.1	26	11.146 (1603)	21.702 (3121)	10.779 (8736)	0.0	101.1 ± 5.5	24.42	122	13.09 ± 0.15	1.70	14.42 ± 1.13	104	1.95 ± 0.02	0.17
GP6GN3.2	31	8.15 (1716)	21.22 (4468)	10.851 (8736)	83	76.6 ± 2.5	22.47	128	13.13 ± 0.11	1.21	14.63 ± 0.89	124	1.95 ± 0.01	0.17
GP6GN3	22	13.169 (1644)	26.834 (3350)	10.94 (8736)	72.5	98.6 ± 3.4	28.11	183	12.70 ± 0.20	2.40	14.19 ± 1.31	88	1.88 ± 0.02	0.20
GP15/16	18	3.331 (334)	57.397 (5755)	10.833 (8736)	17.7	11.6 ± 0.8	63.19	105	12.97 ± 0.25	2.59	14.37 ± 1.61	80	1.79 ± 0.02	0.15
GP9S6	25	2.071 (315)	15.263 (2321)	10.726 (8736)	76.5	26.9 ± 1.7	16.39	44	11.10 ± 0.41	2.71	13.08 ± 1.63	108	1.55 ± 0.01	0.13
GP13/14S10[b]	24	1.085 (195)	25.243 (4536)	10.761 (8736)	97.8	8.6 ± 0.6	27.27	46	13.89 ± 0.26	1.77	14.98 ± 1.04	96	1.66 ± 0.02	0.18
GP15S11[b]	19	1.798 (146)	28.117 (2283)	10.815 (8736)	99.6	12.8 ± 1.1	29.39	27	12.54 ± 0.56	2.90	14.29 ± 1.73	88	1.61 ± 0.02	0.16
GP11S8[b]	25	0.904 (125)	18.394 (2544)	10.922 (8736)	76.3	9.7 ± 1	19.36	10	13.29 ± 1	3.16	14.74 ± 1.68	68	1.66 ± 0.02	0.20
GP13GN9[b]	24	1.193 (174)	22.382 (3265)	10.797 (8736)	82.5	10.6 ± 0.9	25.06	58	12.82 ± 0.33	2.53	14.39 ± 1.33	96	1.59 ± 0.02	0.17

[a]Abbreviations: N, number of individual grains dated per sample; ρs, spontaneous track density; Ns, number of spontaneous tracks counted; ρi, induced track density in external detector (muscovite); Ni, number of induced tracks counted; ρd, induced track density in external detector adjacent to dosimetry glass; Nd, number of tracks counted in determining ρd; and P(χ^2), chi-square probability, Trackkey software [*Dunkl*, 2002] was used for calculating the central fission track ages ±1σ. Samples were processed by Alexander Grist at Dalhousie University (Halifax, Canada) and analyzed by I. Coutand at the Université de Lille (France); standard magnetic and heavy liquid mineral separation procedures were used. Apatites were mounted in araldite epoxy. Sample surfaces were ground and polished. Apatite mounts were etched in 5M HNO3 at 24°C for 20 s. An "external detector" [*Naeser*, 1976], consisting of low-U (<5 ppb) muscovite, was used for each sample. Samples were irradiated at the Dalhousie University Slowpoke reactor. Following irradiation, the muscovites were etched in 48% HF for 30 min at room temperature. Tracks were counted using a 100× dry lens and 1250× total magnification in crystals with well-etched, clearly visible tracks and sharp polishing scratches. A Kinetek stage and software [*Dumitru*, 1993] were used for analyses. Standard and induced track densities were determined on external detectors (geometry factor = 0.5), and spontaneous track densities were determined on internal mineral surfaces. Ages were calculated using ζ = 369.5 ± 5.1 for dosimeter glass CN5 for I. Coutand.

[b]A ^{252}Cf-irradiated grain mount was made to increase the number of measurable track lengths.

Table 5. Summary of Apatite Fission Track Thermal Modeling Results

Sample	GP6GN3.3	GP6GN3.2	GP6GN3	GP15/16 First Set	GP15/16 Second Set	GP13/14S10 First Set	GP13/14S10 Second Set	GP15S11 First Set	GP15S11 Second Set	GP13GN9 First Set	GP13GN9 Second Set
First constraint	100°–160°C 110–120 Ma	100°–160°C 110–120 Ma	100°–160°C 120–140 Ma	10°–40°C 60–80 Ma	10°–40°C 60–80 Ma	10°–40°C 60–80 Ma	10°–40°C 60–80 Ma	10°–40°C 60–80 Ma	10°–40°C 60–80 Ma	10°–40°C 60–80 Ma	10°–40°C 60–80 Ma
Second constraint	10°–40°C 60–80 Ma	10°–40°C 60–80 Ma	10°–40°C 60–80 Ma	100°–160°C 10–35 Ma	100°–160°C 10–35 Ma	100°–160°C 10–35 Ma	100°–160°C 10–35 Ma	100°–160°C 10–35 Ma	100°–160°C 10–35 Ma	100°–160°C 10–35 Ma	100°–160°C 10–35 Ma
Third constraint	35°–80°C 3–35 Ma	35°–65°C 3–35 Ma	35°–65°C 3–35 Ma	10°–20°C present	10°–25°C 1–10 Ma	10°–20°C present	10°–25°C 1–10 Ma	10°–20°C present	10°–25°C 1–10 Ma	10°–20°C present	10°–25°C 1–10 Ma
Fourth constraint	10°–20°C present	10°–20°C present	10°–20°C present	...	10°–20°C present	...	10°–20°C present	...	10°–20°C present	...	10°–20°C present
Paths	32,026	112,577	101,596	9793	41,166	28,445	24,304	11,924	17,626	32,267	25,563
Acceptable fits	761	1507	10174	519	878	743	724	2073	3426	3896	1513
Good fits	100	100	20	100	100	100	100	500	500	500	100
Oldest track, Ma	90	86.8	114	15.2	14	8.9	8.9	14.6	14.7	12.7	13.3
T_A, °C	124	121	118	127	135	126	128	115	114	119	110
Late Cretaceous cooling rate, °C/km	5.4	4.8	2.3	...	...	...	...	...	...	...	...
Late Cretaceous exhumation rate, mm/a	[0.18–0.27]	[0.16–0.24]	[0.08–0.12]	...	...	...	...	...	...	...	...
Peak of reheating (Tertiary burial), °C	70	55	50	...	...	...	...	...	...	...	...
Start of late Tertiary cooling, Ma	[5–15]	[5–15]	[5–10]	15.2	14	8.9	8.9	14.6	14.7	12.7	13.3
Late Tertiary cooling rate, °C/Ma	[3.6–11]	[2.6–8]	[3.5–7]	7.4	12	12.4	28.9	6.8	11.4	8.2	9.7
Late Tertiary exhumation rate, mm/a	[0.12–0.55]	[0.09–0.4]	[0.12–0.35]	[0.24–0.37]	[0.4–0.6]	[0.41–0.62]	[0.96–1.44]	[0.23–0.34]	[0.38–0.57]	[0.27–0.41]	[0.32–0.48]
Thickness of eroded crustal column, km	1.8–2.75	1.3–2	1.15–1.75	3.6–5.6	4–6	3.7–5.6	3.75–5.6	3.3–4.9	3.3–4.9	3.4–5.2	3.1–4.7
Earliest exposed at the surface at, Ma	...	...	...	...	4–5 Ma	...	5.5–5	...	5.5	...	3.5

minerals, which creates a linear damage zone (a fission track) in the crystal lattice. For apatite, tracks begin to be retained at temperatures below $\sim 120^\circ - 150^\circ$C, depending on the cooling rate and the kinetic characteristics of the crystal [e.g., *Green et al.*, 1985; *Ketcham et al.*, 1999]. Determining the density of spontaneous fission tracks and the concentration of ^{238}U yields a single-grain fission track age [e.g., *Naeser*, 1976]. Fission tracks are unstable features that shorten (anneal) by thermal and time-dependent recrystallization processes. Over geological timescales, significant track shortening occurs in fluorine-rich apatite between 60° and 110°C [e.g., *Donelick et al.*, 1999; *Laslett and Galbraith*, 1996; *Laslett et al.*, 1987]; this temperature range is called the partial annealing zone (PAZ) [*Gleadow and Duddy*, 1981; *Green et al.*, 1986]. At sufficiently low temperatures, both old and new tracks are fully retained in the crystal, whereas at increasing temperatures within the PAZ, newly formed tracks are long and older tracks are progressively shortened. Therefore a track-length distribution is a measure of the time spent within and below the PAZ. Interpretation of a fission track data set in terms of a T-t path requires an integrated analysis of fission track age, confined track-length distribution and kinetic characteristics of apatite grains (for overviews, see *Donelick et al.* [2005], *Ketcham* [2005], and *Tagami and O'Sullivan* [2005]).

[17] Between 18 and 31 good quality grains per sample were selected and dated in this study. For track length analysis, all available horizontal confined tracks and the angle between each track and the crystal's *c* axis were measured in each sample. To characterize the annealing properties of the apatites [*Donelick et al.*, 1999; *Ketcham et al.*, 1999], at least four Dpar measurements (when available) were averaged from each analyzed crystal. Both track length and Dpar measurements were calibrated against Durango values reported by *Donelick et al.* [1999].

4.2. Analytical Results

[18] The five samples collected from the southernmost part of the Shillong plateau, west of the NE-SW-trending Badapani-Tyrsad shear zone, yielded apatite fission track (AFT) central ages between 8.6 ± 0.6 Ma and 12.8 ± 1.1 Ma (Figures 2 and 4 and Table 4). Dpar values between 1.59 ± 0.02 μm and 1.79 ± 0.02 μm, and their low standard deviation ($\leq$0.20 μm), indicate that these samples contain apatite crystals with similar annealing behaviors. All samples passed the χ^2 test, meaning that the single-grain ages are consistent with a common age for each sample. Mean track-length values range between 12.54 and 13.89 μm with standard deviation between 1.77 and 2.90 μm (see Table 4 and Figure 4).

[19] The four samples collected north of the Oldham fault (Figure 2), yielded much older and more scattered AFT ages, between 75 ± 2.7 and 101.1 ± 5.5 Ma (Figure 4 and Table 4). Sample GP6GN3.1 did not pass the χ^2 test indicating extra dispersion in the data, and will not be considered any further. Dpar values range from 1.85 ± 0.01 μm to 1.95 ± 0.02 μm suggest that these apatite crystals may be slightly more resistant to annealing than the previous set [*Ketcham et al.*, 1999]. Mean track-length values vary between 11.99 and 13.13 μm with standard deviation between 1.21 and 2.40 μm (see Table 4 and Figure 4).

[20] Mean track length values and associated standard deviations suggest that all samples (both those with late Cretaceous and late Tertiary apparent ages) have resided, to a greater or lesser extent, in the AFT partial annealing zone. Finally, sample GP9S6 collected on the eastern side of the Badapani-Tyrsad shear zone yielded a central age of 26.9 ± 1.7 Ma with the shortest mean track lengths of the data set and a bimodal distribution (Table 4).

[21] Samples from the northern flank of the Shillong plateau yielded Middle to Late Cretaceous apatite (U-Th-[Sm])/He ages. In contrast, apatite (U-Th-[Sm])/He ages of samples from the southern part of the plateau are generally within error equal or slightly younger than the AFT ages. This pattern suggests rapid Middle to Late Miocene cooling from temperatures significantly higher than 70°C. In general there is a good correlation between AFT and (U-Th-[Sm])/He ages, with the oldest samples being found in the north and the youngest in the south of the Shillong plateau (Figure 2). However, in detail (U-Th-[Sm])/He ages should be systematically younger than AFT ages. Such conflicting ages between the two systems have been reported in an increasing number of studies [e.g., *Green et al.*, 2006; *Hendriks and Redfield*, 2005]. It has recently been suggested that such age discrepancies are likely due to variations of the He retention properties of apatite crystals, related to the degree of accumulated radiation damage in the crystal lattice [*Green et al.*, 2006; *Hendriks and Redfield*, 2005]. Hence inconsistencies are likely more pronounced in samples of older FT ages and/or of significant U content. Quantitative description of how α damage changes closure temperature [*Shuster et al.*, 2006] was applied and the effective closure temperature T_{ec} was estimated for all the apatite samples. However, the *HeFTy* software could not produce viable thermal histories even when the corrected apatite He ages and T_{ec} were used. For this reason, we mostly relied on apatite fission track data for reconstruction of the thermal histories of the studied samples.

5. Thermal Modeling

[22] In order to interpret our fission track data set in terms of T-t paths, thermal modeling combining *c* axis projected track lengths, single grain ages, and Dpars was performed using the *HeFTy* program [*Ehlers et al.*, 2005; *Ketcham*, 2005], which implements the annealing model of *Ketcham et al.* [1999]. Seven samples were found suitable for modeling, although for one of them (GP15S11), only 27 horizontal confined-track lengths were measured (Table 4).

[23] Using the Monte Carlo random search, each model run had between 9800 and 112,000 iterations (until the target number of good fits has been achieved; see Table 5) with monotonic path segments and four half-segments evenly spaced between adjacent constraints. Heating and cooling rates were not constrained. For every model run, the program determined the best fit path as well as the good fit

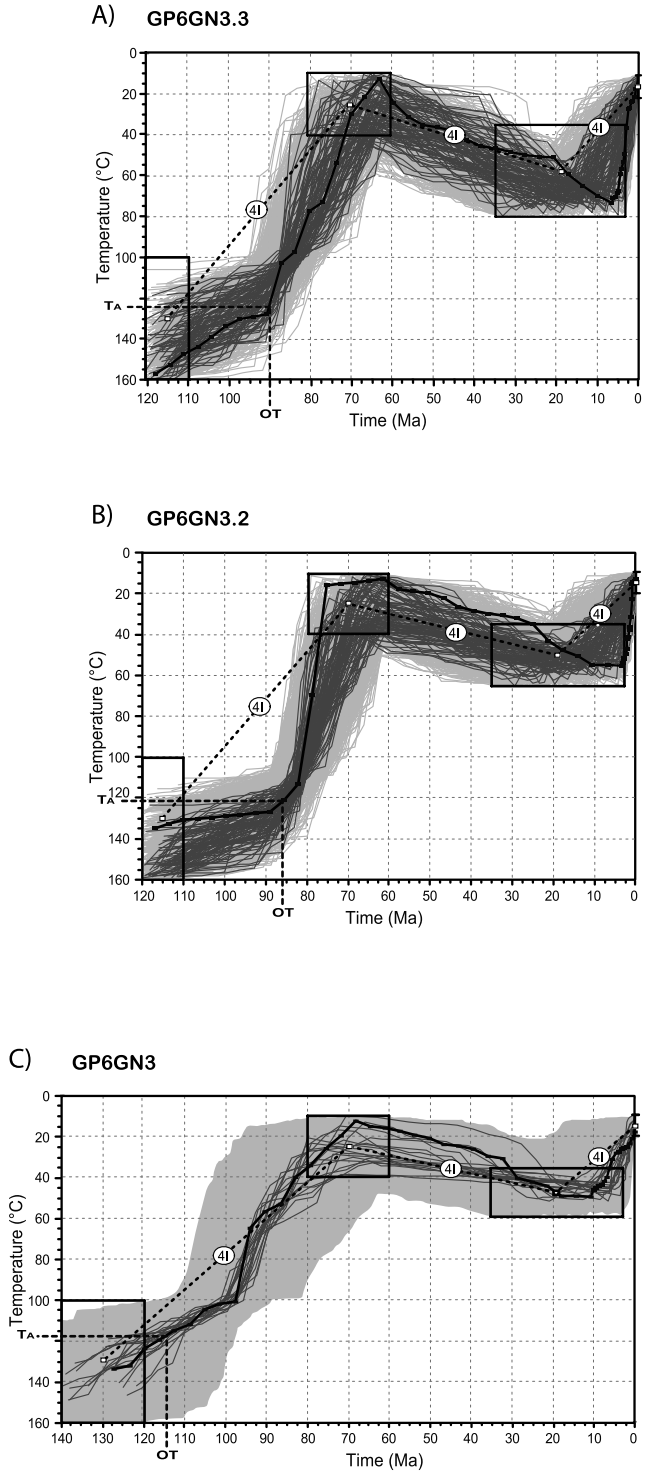

Figure 5. Representative *HeFTy* models for the Shillong plateau (Group 1) samples. The black boxes represent time-temperature constraints. To prevent strong forcing of t-T paths, initial sizes of the boxes were set very large and progressively reduced in order to optimize the search for good fits. Good fit solutions are represented by dark grey paths and acceptable fit solutions by pale grey paths. The thick black line is the best fit t-T path. OT is the oldest track formed at T_A, the total annealing temperature.

and the acceptable fit solutions [*Ketcham*, 2005; *Ketcham et al.*, 2000]. On the basis of their age, track length distributions and locations, the samples were divided into two groups, old samples north of Oldham (Group 1), and younger ones south of it (Group 2) (Figures 4–6).

5.1. Group 1

[24] Four constraints were used for this set of 3 samples (Table 5): (1) (100°–160°C) between 110 and 120 Ma (this corresponds to the activity of the Kerguelen hot spot as documented by the early Cretaceous mafic volcanic and igneous rocks intruding the Proterozoic basement of the plateau and related to this plume event (Figure 2)); (2) (10°–40°C) between 60 and 80 Ma (deposition of continental strata (Maastrichtian) unconformably on the plateau's pre-Cretaceous erosion surface); (3) (35° to 60°–80°C) between 3 and 35 Ma (reburial of the basement beneath Tertiary sediments); and (4) (10°–20°C) as present surface conditions.

[25] Samples GP6GN3.2 and GP6GN3.3 were cooled below their total annealing temperature (T_A) at 87 and 90 Ma, respectively (ages of the oldest tracks extracted from the best fit paths; Table 5), and were progressively cooled at rates between 4.8 and 5.4°C/Ma until the samples reached surface temperatures (15°C) in the late Cretaceous (Figures 5a and 5b). Assuming a paleogeothermal gradient of 20°–30°C/km [*Rao et al.*, 1976; *Zahid and Uddin*, 2005], this early episode yields exhumation rates of 0.16–0.27 mm a^{-1}. From the end of the Maastrichtian, bedrock starts to be progressively reburied by sedimentation from the surface to maximum temperatures of about 55°C for GP6GN3.2 and 70°C for GP6GN3.3 (good-fit solutions, Figures 5a and 5b). Samples GP6GN3.2 and GP6GN3.3 underwent increases in temperature ranging from 40° to 55°C respectively, suggesting burial under an ~1.3- to 2.75-km-thick sedimentary section. According to good-fit solutions, onset of the final exhumation is possible anytime between 3 and 25 Ma, but started most likely between 5 and 15 Ma (Figures 5a and 5b), yielding late Tertiary exhumation rates between 0.09 and 0.55 mm a^{-1}. The crustal column thickness removed from above the bedrock samples ranges between 1.3 and 2.75 km and is mostly composed of Tertiary sediments. Sample GP6GN3 has an older apparent age of 98.6 ± 3.4 Ma, and yielded similar results to those described above, although with fewer good fits (see Figure 5c and Table 5).

5.2. Group 2

[26] Three time-temperature constraints were applied to this set of four samples (Table 5): (1) (10°–40°C) between 60 and 80 Ma (deposition of continental strata (Maastrichtian Stage) unconformably on the plateau's pre-Cretaceous erosion surface); (2) (100°–160°C) between 10 and 35 Ma (reburial of the basement beneath Tertiary sediments); and (3) (10°–20°C) as present surface conditions.

[27] The oldest tracks extracted from the best fit paths were formed between 15.2 and 8.9 Ma, indicating that the samples started to cool from below their total annealing temperature (T_A) at that time. t-T paths indicate uniform

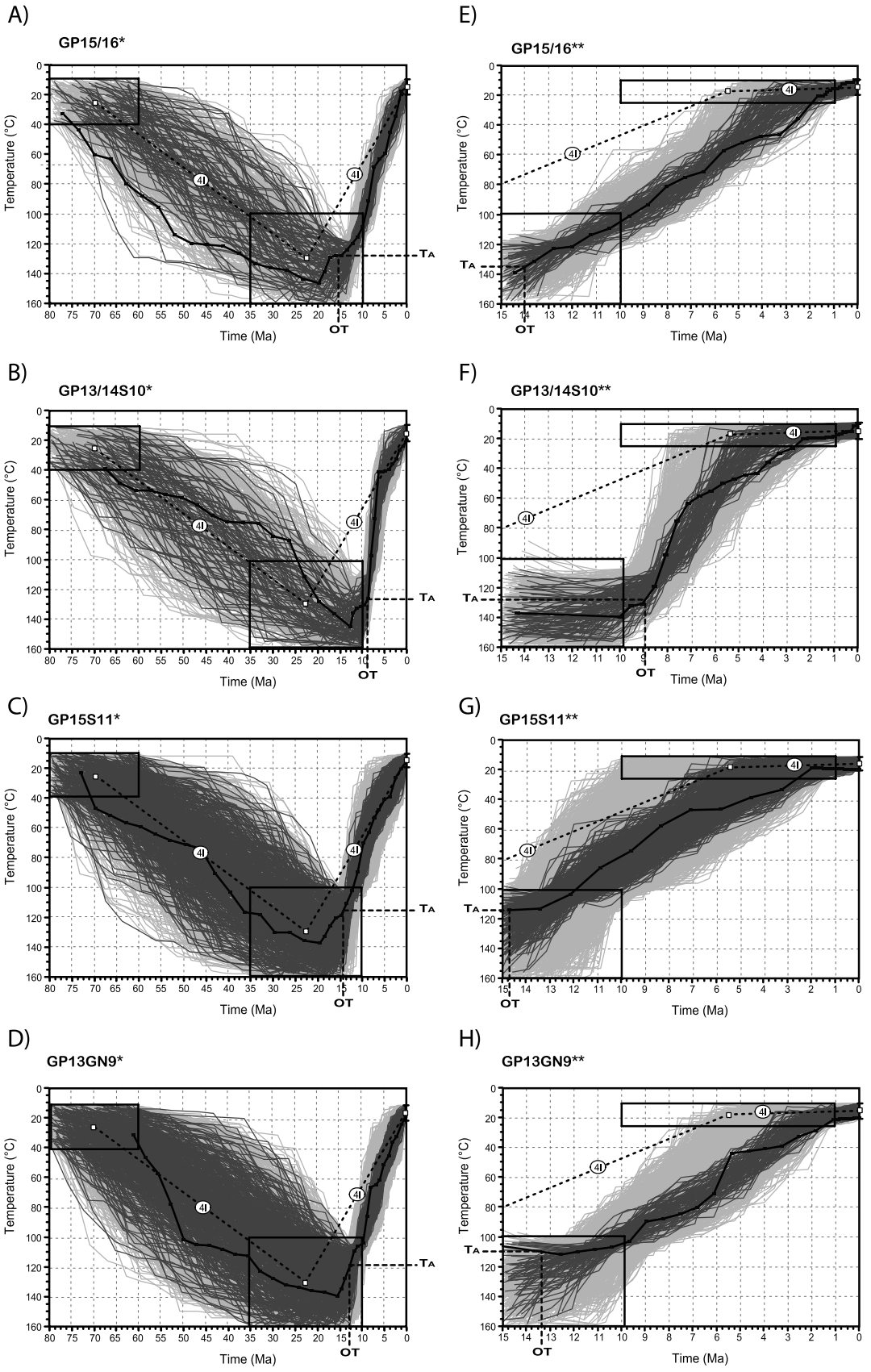
A)
GP15/16*
B)
GP13/14S10*
C)
GP15S11*
D)
GP13GN9*
E)
GP15/16**
F)
GP13/14S10**
G)
GP15S11**
H)
GP13GN9**
Temperature (°C)
Time (Ma)
TA
OT
4I

Figure 6

cooling rates between 6.8 and 12.4°C/Ma (Figures 6a–6d and one-star models in Table 5). Assuming a geothermal gradient of 20°–30°C/km and uniform cooling up to the surface, this yields exhumation rates between 0.23 and 0.62 mm a^{-1} (Table 5). Inferred minimum crustal column thickness removed from above the bedrock samples is 3.3–5.6 km and the bulk of the eroded section is composed of Tertiary sediments.

[28] Finally, in order to examine whether these bedrock samples may have undergone nonuniform cooling, and in particular, may have been exposed at the surface earlier than the present, a set of models was performed involving an additional t-T constraint at 10°–25°C between 1 and 10 Ma (Figures 6e–6h; two-stars models in Table 5). By forcing the samples toward the surface earlier than the present, we obtained good fits for all four samples and it appears that they may have reached the surface as early as, or anytime after 3.5–5.5 Ma (Figures 6e–6h).

6. Discussion

[29] The Indian Summer Monsoon (ISM) plays an essential role in the erosion along the southern flank of the Himalaya [*Bookhagen et al.*, 2005]. The onset of ISM is believed to have taken place by 12–10.7 Ma [*Dettman et al.*, 2003, 2001]. In eastern Bhutan, the ISM precipitation is influenced by the Shillong Plateau, the only elevated terrain outboard of the entire Himalayan orogen. The E-W oriented Shillong plateau forms an ~1600-m-high orographic barrier to the prevailing winds transporting moisture from the Bay of Bengal toward the Himalayan front [*Bookhagen et al.*, 2005]. Consequently, the foothills of eastern Bhutan in the lee receive about half the precipitation as Himalayan foothills outside the rain shadow. The recent precipitation pattern [*Bookhagen et al.*, 2005; *Grujic et al.*, 2006] was likely developed when the plateau had attained sufficient elevation to cause the orographic effect. It was suggested that the Shillong plateau was submerged under the sea until the Mio-Pliocene transition (6–4 Ma ago), and that it has emerged during the Pliocene [*Johnson and Alam*, 1991; *Uddin and Lundberg*, 2004]. Therefore the reorganization of the precipitation distribution in Bhutan due to uplift of the Shillong plateau occurred after the ISM was enduringly established along the Himalaya. Accordingly, it is reasonable to assume that, until the end of the Miocene, the eastern Bhutan, currently located in the lee of the Shillong plateau, received much higher rainfall than today. As a consequence the eastern and western Bhutan Himalayas show contrasting erosions histories, surface landscapes, and structures in the Earth's crust. It is suggested [*Grujic et al.*, 2006] that the spatiotemporal variations of the landscape and the tectonic structures in the eastern Himalaya are a response to climate-driven changes in erosion rates. To test and quantify these hypotheses it is imperative to determine: (1) the onset of the exhumation of the Shillong plateau; (2) the amount of N-S shortening taken up by the plateau-bounding faults, i.e., degree of partitioning of India-Asia convergence between the Shillong plateau and the Bhutan Himalaya; and (3) timing and rate of its surface uplift, i.e., to determine when the orographic barrier was created.

6.1. Thermal Histories and Exhumation

[30] The AFT data are clearly an expression of the underlying thermal histories. Importantly, the bedrock samples from Group 2 were collected at the top of a low-relief, flat paleosurface cut into the basement rocks (Figures 1, 2, and 7a). This paleosurface was probably formed at the end of the Paleozoic as indicated by zircon (U-Th)/He ages, or at least before the Late Cretaceous. In fact, Late Cretaceous-Paleogene sediments were deposited directly and unconformably on this surface [see *Evans*, 1964, Figure 1b] that projects parallel to the top of the southern plateau (Figure 7b). Farther north, this surface is slightly tilted toward the north (Figure 1), with mean elevations of about 1600 m being observed in its southern part (Figure 7a). The evenness of this basement/sediment interface (Figure 1) and the presence of remnants of Paleogene sediments at the top of the plateau (Figure 2) indicate that this surface has not been eroded much, if at all. Basement erosion seems to be focused on the steep southern flanks of the plateau with the jagged southern margin of the plateau representing the northward propagating erosional front.

[31] All the rocks in the study area were likely exposed at the surface in the late Cretaceous. The main difference between the two groups of samples is that in the early Tertiary, the bedrock samples from Group 1 were reburied under a minor sedimentary cover thin enough to preserve their pre-Tertiary He and AFT thermal histories; while the samples from Group 2 were exposed at the surface and then buried and reheated to a level sufficient to reset the AFT clock, removing any earlier thermal history information. Importantly, the timing of the onset of exhumation, the thickness of denuded sections and the exhumation rates are derived from thermal modeling of AFT data. The AFT data only constrain a portion of the total cooling history, which might have started earlier and at a greater depth. Consequently, in case of totally reset samples, sedimentary thicknesses and exhumation rates are minimum estimates. However, the preservation of Paleozoic zircon (U-Th)/He ages on the paleosurface indicates that Tertiary burial depth could not exceed 5.1–8.75 km assuming a zircon (U-Th)/He thermochronometer closure temperature of 170°–190°C [*Reiners et al.*, 2004] and a paleogeothermal gradient of 20°–30°C/km in the Tertiary sediments [*Rao et al.*, 1976; *Zahid and Uddin*, 2005].

[32] South of the Oldham fault, the sedimentary column under which the paleosurface was initially buried is calculated to be at least 3.3–5.6 km thick (Table 5 and Figure 7). Provided final exhumation started between 15.2 to 8.9 Ma ago, this yields minimum long-term exhumation rates of

Figure 6. Representative *HeFTy* models for the Shillong plateau (Group 2) samples; same legend as for Figure 5. The stars indicate the different third constraint used in the models (one star is the first set and two stars is the second set) (see Table 5).

0.23–0.62 mm a^{-1} (see Table 5). Within error, this value is similar to the average denudation rate along the northern slope of the Shillong plateau estimated from sediment yields at 1.0 ± 0.5 mm a^{-1} [*Garzanti et al.*, 2004].

[33] North of the Oldham fault, the thickness of the sedimentary column removed from above the bedrock samples is between 1.15 and 2.75 km (Figure 7). The late Tertiary exhumation episode started between 5 and 15 Ma,

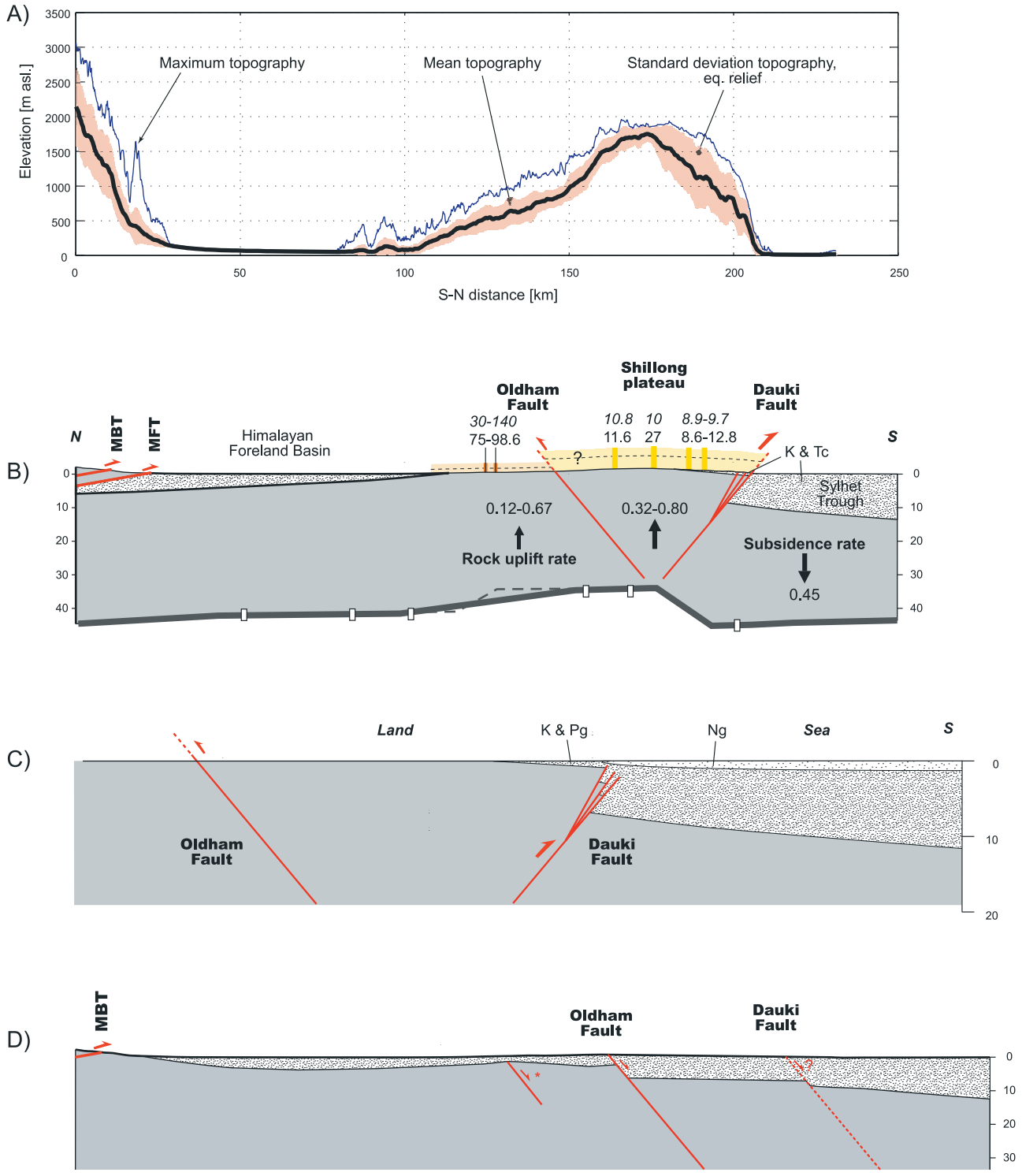

Figure 7

yielding long-term exhumation rates between 0.09 and 0.55 mm a^{-1} (see Table 5).

6.2. Vertical Displacements Along the Oldham and Dauki Faults

6.2.1. Dauki Fault

[34] The continuous subsidence of the southern block of the Dauki fault has resulted in the Sylhet trough, with at least 18 km of sediments deposited since the Cretaceous [*Alam et al.*, 2003; *Johnson and Alam*, 1991] (Figure 1). The structural relief between the highest part of the Shillong plateau (mean elevation of 1600 m) and the basement in the deepest part of the Sylhet trough is estimated to be around 15–19 km [*Hiller and Elahi*, 1984; *Shamsuddin and Abdullah*, 1997]. However, the sedimentary thickness against the Dauki fault is "only" ~10 km [*Shamsuddin and Abdullah*, 1997] (Figure 1). Therefore the fault may have a long history of activity, acting since Late Cretaceous as a south-dipping normal fault in the developing continental margin of SE India, and accommodating more sediment thickness in the hanging wall to the south than in the footwall in the north (Figure 7d). Conversely, the isopach map (Figure 1) indicates that the basement flooring the Sylhet trough is gently inclined southward (~5°), which is identical to the dip of the basement-Cretaceous strata interface on the southern margin of the Shillong plateau (Figure 7b). Therefore the here estimated difference in thickness of Tertiary sediments between the top of the Shillong plateau and the northern margin of the Sylhet trough (maximum ~6–8 km versus ~10 km) may be explained by the gently south-dipping basement and thus northward tapering of the Tertiary sedimentary cover. The reverse south-verging Dauki fault might thus have formed at the onset of the exhumation, which is mechanically easier than reactivating an initial south-dipping normal fault. In summary, the total vertical displacement of the basement top along the Dauki fault is ~10 km (assuming no initial normal fault displacement) yielding a mean vertical displacement rate of 0.66–1.11 mm a^{-1} if it has been active as a reverse fault since the onset of the late Tertiary exhumation as recorded by AFT analysis, i.e., 8.9 to 15.2 Ma ago.

[35] To better constrain the vertical displacement rate along the Dauki fault during the late Tertiary, the subsidence of the footwall, i.e., the Sylhet trough [*Uddin and Lundberg*, 2004; *Worm et al.*, 1998], should also be taken into account. The youngest marine sediments recognized on the southern foothills of the Shillong plateau, the Early Pliocene Boka Bil formation of the Surma group, are also observed in a drill hole in northern Bangladesh, south of the Dauki fault (Figure 2). The base of this unit is at a depth of −1081 m, and the top at −626 m [*Uddin and Lundberg*, 2004]. The age of the Boka Bil formation was determined by magnetostratigraphy and is bracketed between 4.4 and 3.4 Ma [*Worm et al.*, 1998], which gives a subsidence rate of 0.45 mm/a during its deposition in this area.

[36] To constrain the late Tertiary vertical displacement rate of the block located north of the Dauki fault (Shillong plateau) we use AFT modeling results, which suggest that the minimum sedimentary thickness removed from the top of the Shillong plateau during the Late Miocene-Pliocene was between 3.3 and 5.6 km. Given that the basement was not eroded during this exhumation episode and that the pre-15 Ma Tertiary sediments were all marine, the sedimentary thickness corresponds to the basement depth beneath the sea level when exhumation started ~15 Ma ago. Note that the depth to the basement could not exceed ~ 8 km, because otherwise it would have been deeper than in the Sylhet trough (Figure 7b), and the Paleozoic zircon He ages would have been reset. The uplift of the basement surface to the modern plateau's mean elevation (1.6 km) since 8.9–15.2 Ma is therefore at least ~ 4.9–7.2 km (but less than ~9.6 km). Hence the rock uplift rate in the hanging wall of the Dauki fault ranges between 0.32 and 0.80 mm a^{-1}. Accordingly, the combined mean vertical displacement rate along the Dauki fault ranges between 0.77 and 1.25 mm a^{-1},

Figure 7. (a) Topographic swath profile with 36x vertical exaggeration showing the principal topographic features of the Shillong plateau. Note that the relief along the southern flank of the plateau is much larger (700–900 m) than at the top (200–300 m). The activity of the Oldham fault is suggested by the break in slope observed at its intersection with the surface topography. (b) N-S cross section at 91°40′E ± 10′. The thickness of the sediments in the Sylhet trough is based on work by *Shamsuddin and Abdullah* [1997]. Position and attitude of the Dauki and Oldham faults are after *Bilham and England* [2001]. The position of the Moho (white boxes) is based on data from *Mitra et al.* [2005]. Original interpretation is given by grey dashed line, and suggested interpretation is given by heavy grey line. Dip to the north of 3°–4° both of the Moho and of the top of the basement is consistent with the estimates of the position of the Moho without the necessity for a northern step related to the Oldham or Brahmaputra [*Rajendran et al.*, 2004] faults. This geometry is also consistent with the northward thickening of Tertiary-Quaternary sediments to ~5 km in the Brahmaputra Basin [*Rath et al.*, 1997; *Singh et al.*, 1998; *USGS-Bangladesh Gas Assessment Team*, 2001]. Sample locations are indicated with the corresponding ages: Numbers in regular font are the apatite fission track central ages, and numbers in italics are the apatite (U-Th-[Sm])/He ages. Colored bars in yellow (light brown) correspond to the maximum thickness of the sedimentary cover deduced from thermal modeling of AFT data for samples from Group 2 (Group 1) and now eroded. Dashed lines indicate the minimum thickness estimate. (c) Most likely geometry of faults and landscape at the onset of the surface uplift of the Shillong plateau in the Early Pliocene. (d) Schematic N-S section across the Shillong plateau at the time of the onset of the exhumation of the basement. Oldham fault and likely Dauki faults were basinward (southward) dipping normal faults. A southwest dipping normal fault indicated by an asterisk has been observed in the northern plateau (A. Yin, personal communication, 2007).

which is in agreement with the values (0.66–1.11 mm a^{-1}) calculated from the basement offset (see section 6.1).

6.2.2. Oldham Fault

[37] In terms of thicknesses of Tertiary depocenters, the regions located north and south of the Oldham fault are fundamentally different with respectively 1.25–2.75 km and 3.3–5.6 km of Tertiary sediments formerly overlying the basement as documented by AFT data (Figure 7b). Hence we suggest that the Oldham Fault is a major paleogeographic boundary. In particular, during the Late Cretaceous it has likely acted as a south-dipping normal fault developed during the breakup of India and Antarctica and as a part of the then newly formed continental margin of India (Figure 7c). The footwall of the normal fault was rapidly exhumed at that time, as shown by apatite FT and (U-Th-[Sm])/He Late Cretaceous ages. This normal fault was reactivated as a north-directed reverse fault in the context of the India-Eurasia collision.

[38] AFT modeling results suggest that in the footwall of the Oldham Fault, thickness of marine sediments removed from the top of the basement during the late Miocene-Pliocene exhumation is between 1.15 and 2.75 km. Assuming that the incision of the basement is not higher than the modern relief, then the mean elevation of this area (600 m above sea level), can be approximated to the location of the Precambrian basement/Tertiary sediments interface (Figure 7a). Therefore, at the onset of the final exhumation 5 to 15 Ma ago, this interface was located at least at ~1.75–3.35 km beneath the sea level. These observations yield a rock uplift rate of 0.12–0.67 mm a^{-1} in the footwall of the Oldham fault. Considering the rock uplift rate calculated in the hanging wall of this fault (0.32–0.80 mm a^{-1}), and the fact that it is a reverse fault, the mean vertical displacement rate on the Oldham fault averaged over the last 5–15 Ma is 0–0.68 mm a^{-1}.

6.3. Partitioning of the India-Asia Convergence Into the Shillong Plateau

[39] The degree of strain partitioning is relevant to issues regarding the seismic hazard potential of the Shillong plateau and the interval between major earthquakes in the Bhutan Himalaya [*Bilham and England*, 2001]. Furthermore, over extended geological periods of time (~10^7 a) significant partitioning of the India-Eurasia convergence across the Shillong plateau would have major tectonic implications for the Bhutan Himalaya to the north, by reducing the shortening rate and hence the rock uplift rate across this eastern segment of the orogen. In particular, the recently documented difference in exhumation rates between western and eastern Bhutan could be the consequence of a differential horizontal shortening caused by Neogene displacements on Dauki and Oldham faults rather than a climatic modulation of erosion as proposed by *Grujic et al.* [2006].

[40] On the basis of published geological information, *Bilham and England* [2001] estimated the vertical displacement rate (i.e., tectonic uplift) of the Shillong plateau to 2.5 ± 1 mm a^{-1}, and the cumulative horizontal shortening rate to 4 ± 2 mm a^{-1} assuming a fault dip of 50° and equal finite displacement along the two bounding faults. This would suggest that, at the higher end of slip rates estimated by *Bilham and England* [2001], the faults bounding the Shillong plateau could absorb up to one third of the inferred Himalayan contraction rate of 15–20 mm/a [*Zhang et al.*, 2004]. This absorption of contraction within the Shillong plateau leaves less of the convergence rate to be taken up within the Bhutan Himalaya. GPS measurements from 1997–1999 indicated that the active convergence between the central Shillong plateau and the points in central and southern India is 6.3 ± 3.8 mm a^{-1} [*Paul et al.*, 2001], in agreement with the above statements. However, more recent GPS measurements of more stations and over a longer period indicate that in the Indian reference frame, the motion of Shillong is "negligible" [*Jade*, 2004].

[41] The long-term vertical displacement rates on the Oldham and Dauki faults determined in this study are 0–0.68 mm a^{-1} and 0.77–1.25 mm a^{-1} respectively. Assuming a dip of 40°–50° for both faults (expounded by *Bilham and England* [2001]), the mean shortening rate accommodated by the Oldham Fault ranges between 0–0.8 mm a^{-1} and by the Dauki Fault between 0.65 and 1.5 mm a^{-1}. Consequently, the mean cumulative shortening rate across the Shillong plateau since the Late Miocene is between 0.65 and 2.3 mm a^{-1}. The upper value corresponds to the lower end of the cumulative horizontal shortening rate proposed by *Bilham and England* [2001] and is less than 10–15% of the Himalayan contraction rate.

[42] Our results clearly document that the long-term horizontal shortening accommodated by the Shillong plateau is minor and consequently that in the Bhutan Himalaya there was no significant change in horizontal shortening and in rock uplift rate caused by the Shillong plateau development since the onset of its exhumation 9–15 Ma ago. Therefore the gradient in erosion rates observed across Bhutan is primarily attributed to a climatic modulation as previously suggested by *Grujic et al.* [2006].

6.4. Surface Uplift of the Shillong Plateau

[43] Surface uplift of the Shillong plateau either might have occurred at uniform rate since about 15 Ma or more likely might have been chronologically decoupled from the exhumation of the basement of the plateau. In the first case, surface uplift rate is uniform and corresponds to the mean exhumation rate (0.23–0.62 mm a^{-1}) subtracted from the mean rock uplift rate (0.32–0.80 mm a^{-1}) [*England and Molnar*, 1990] during the last 15 Ma yielding a long-term surface uplift rate of 0–0.57 mm a^{-1}. In the second case, the contrast in rock erodibility between the Tertiary marine sediments overlying the well-preserved and exposed flat pre-Cretaceous paleosurface, carved into resistant Precambrian bedrock, induced a temporal decoupling between exhumation and surface uplift of the Shillong plateau. Initially, the sediments were removed owing to their high erodibility causing fast bedrock cooling and slow surface uplift. Once the more resistant bedrock was exposed, erosion may have drastically slowed, resulting in the conversion of rock uplift into surface uplift (± isostatic compensation). Such processes have been previously

documented elsewhere [e.g., *Sobel and Strecker*, 2003]. The question is, when and at which elevation did this transition occur? The answer to this question would be simplified if the surface exposure of the basement/sediment interface could be dated, and if it were possible to determine its position with respect to the sea level at that time. Unfortunately, we do not have these information, however the climatically induced change in erosion rate "sometimes after 5.9 Ma" along the Himalayan front in Eastern Bhutan documented by *Grujic et al.* [2006] can serve as a temporal guide. In our AFT data modeling, we tested the hypothesis of decoupled exhumation/surface uplift by adding a t-T constraint forcing the bedrock samples toward the surface earlier than the present (see end of section 5.2 and Figures 6e–6h). Results suggest that the four samples may have reached the surface anytime between 5.5 and 3.5 Ma (good fits) (Figures 6e–6h and Table 5). Furthermore, the sedimentation on the southern foothills of the Shillong plateau was marine until 3–4 Ma, thus it is unlikely that significant topography started to be built before then. The maximum mean modern elevation of the plateau is $\sim$ 1.6 km (Figure 7a). If the emersion of the plateau coincides with the exposure of its Precambrian basement, then the maximum mean surface uplift rate of the plateau is between 0.4–0.53 mm a^{-1} during the last 3–4 Ma. If this hypothesis is correct, then the entire sedimentary column was removed by erosion between 8.9–14.7 and 3.5–5.5 Ma at rates of 0.32–1.44 mm a^{-1} (see Figures 6e–6h and Table 5). A better knowledge of the age and distribution of the youngest marine sediments deposited on the plateau is still needed to evaluate more accurately the surface uplift rate of the Shillong plateau.

6.5. Causes of the Development of the Shillong Plateau

[44] The Shillong plateau was built as a result of contractional deformation due to the Indo-Eurasia collision. However, its exhumation (and hence reverse displacements on its bounding faults) as recorded by our low-temperature thermochronometers, initiated only 9–15 Ma ago. According to the zircon (U-Th)/He nonreset Paleozoic ages, and assuming the exhumation rates documented by AFT data in the southern part of the Shillong plateau were steady, the onset of exhumation driven by the Dauki Fault cannot be older than 25 to 35 Ma (uniform exhumation) and 20–30 Ma (nonuniform exhumation) (for a closure temperature of 180°C, a surface temperature of 15°C and a geothermal gradient of 20°–30°C/km). Nevertheless, the thermal modeling of AFT data from the northern portion of the Plateau (Group 1) of partially reset samples, indicates that the onset of exhumation, driven primarily by displacements on the Dauki fault, did not start before 5–15 Ma. Only the identification and dating of unconformities and provenance analyses in the sedimentary filling of the Sylhet trough would tightly bracket the onset of the exhumation of the Shillong plateau.

[45] Why did the preexisting normal faults associated with this passive margin invert so late? The causes for the plateau formation are uncertain, but the two most likely possibilities are as follows.

[46] 1. The plateau spatially coincides with a culmination of a gentle bulge in the crust that extends along the foreland basin in the NE India [*Rath et al.*, 1997; *Singh et al.*, 1998]. The Himalayan orogen to the north is associated with a major peripheral foreland basin filled with Neogene to Quaternary sediments [*Najman*, 2006]. To the south of it is a flexural bulge in the Indian crust, discernable topographically only in the central 30° of the Himalayan arc, while the evidence for it is absent at the longitude of Bangladesh [*Bilham et al.*, 2003]. The wavelength, amplitude and distance to the Himalayan frontal thrust of the flexural bulge [*Bilham et al.*, 2003] and the NE Indian bulge are, however, significantly different. Thus a genetic link to the flexural bulge in the foreland of the Himalaya cannot be ascertained.

[47] 2. The encroachment of the Indo-Burman (or Arakan) ranges onto the Bengal basin throughout the Neogene [*Copley and McKenzie*, 2007; *Uddin and Lundberg*, 2004; *Socquet et al.*, 2006] may also have influenced the change in tectonics of the Shillong plateau and its bounding faults.

7. Conclusions

[48] 1. The Indian basement exposed in the Shillong plateau was located at the continental margin of India formed during the break up with Australia and Antarctica. The major faults now bounding the plateau may have acted as normal faults accommodating south to southeastward thinning of the continental crust and controlling sedimentation dynamics in the area. The Shillong plateau subsided more slowly than the Sylhet trough during Cretaceous to Miocene times. As a result, the sedimentary thickness on the top of the plateau probably did not significantly exceed 6000 m while to the north of the Oldham fault it was less than $\sim$ 2750 m. This abrupt northward change in thickness of Tertiary sediments is consistent with progressive attenuation of the crust toward the south (Figure 7b).

[49] 2. Basement exposed at the top and part of the north slope of the Shillong plateau is an ancient erosion surface on which late Cretaceous to Tertiary sediments were deposited. Since the removal of the sediments, the erosion of the basement was minimal. The exhumation of the basement started at least by $\sim$9–15 Ma as indicated by both apatite (U-Th-[Sm])/He and AFT data, and the consistent thermal histories extracted from all localities. Because our low-temperature thermochronometers record only the latest portion of the total cooling history, the exhumation could have started earlier.

[50] 3. Taking into account the calculated exhumation rates, thickness of the Tertiary sedimentary cover and onset of its removal, we estimate the rate of vertical displacement along the Dauki fault to 0.77–1.25 mm a^{-1}, and along the Oldham fault to 0–0.68 mm a^{-1}. Faster displacement along Dauki than along the Oldham fault has, at least partially, caused 2°–3° northward tilting of the surface of the plateau. This tendency may have been intensified by a larger-scale northward tilting of the Indian crust as a result of its flexure due to tectonic loading induced by crustal thickening of the Himalayan orogen in the north.

[51] 4. Surface uplift of the Shillong plateau might have occurred either at uniform rate of 0–0.57 mm a^{-1} during the last 9–15 Ma or, more likely, accelerated sometime after the Late Cretaceous-Tertiary sedimentary cover was partially or entirely removed and the Precambrian basement emerged from the sea. This event occurred 3–4 Ma ago at the latest, once the youngest and last marine sediments documented along the southern foothills of the plateau were deposited, and yields surface uplift rates of 0.4–0.53 mm a^{-1} during this time span.

[52] 5. Using the same attitude of the faults as suggested by *Bilham and England* [2001], we estimate the mean cumulative horizontal shortening rate to 0.65–2.3 mm a^{-1}. These values are significantly lower than the published values and represent only 10–15% of the Himalayan contraction rate. These results indicate that strain partitioning between the Himalaya and the Shillong plateau is minor and hence that no significant change in shortening and rock uplift rate has occurred in the Bhutan Himalaya since the onset of the exhumation of the Shillong plateau 9–15 Ma ago.

[53] 6. The amount of strain partitioning between India, the Shillong plateau and the Bhutan Himalaya, indicates that the tectonic development of the Shillong plateau did not influence the rock uplift rate in the Bhutan Himalaya. These findings strongly support interpretations previously proposed by *Grujic et al.* [2006] that the change in tectonic, erosion and landscape evolution in the Bhutan Himalaya that occurred sometime after 5.9 Ma was triggered by a local climate change caused by the construction of the Shillong plateau orographic barrier.

[54] **Acknowledgments.** Fieldwork on the Shillong plateau was enabled by the invaluable help provided by the Department of Geological Sciences of Jahangirnagar University, Bangladesh. Stimulating discussions with S. Bonnet, B. Bookhagen, and G. Hilley are greatly appreciated. Also thanked are Andrew Carter, Todd Ehlers, and Paul Kapp for their constructive reviews. Urs Klötzli of Vienna University is acknowledged for his support for mineral separation. I. C. thanks the Fulbright Foundation for providing funding during her stay at Stanford University. The third author acknowledges motivating discussions with the members of the Canadian Institute for Advanced Research. The research was supported by the Austrian Academic Exchange Service (Project-1734-4/EZA/2000 and EZA-Projekt 894/05), the Fonds zur Förderung der wissenschaftlichen Forschung (Austria), the NSERC (Canada), the France-Stanford Foundation, and the NSF (USA).

References

Acharyya, S. K., S. Sinha-Roy, and H. Furnes (1980), Geochemistry and geotectonic implication of basic volcanic rocks in the lower Gondwana sequence (upper Palaeozoic) of the Sikkim Himalayas: Discussion and reply, *Geol. Mag.*, *117*, 621–629.

Acharyya, S. K., N. D. Mitra, and D. R. Nandy (1986), Regional geology and tectonic setting of Northeast India and adjoining region, *Mem. Geol. Surv. India*, *119*, 6–12.

Alam, M. (1989), Geology and depositional history of Cenozoic sediments of the Bengal Basin of Bangladesh, *Palaeogeogr. Palaeoclimatol. Palaeoecol.*, *69*, 125–139.

Alam, M., M. M. Alam, J. R. Curray, M. L. R. Chowdhury, and M. R. Gani (2003), An overview of the sedimentary geology of the Bengal Basin in relation to the regional tectonic framework and basin-fill history, *Sediment. Geol.*, *155*, 179–208.

Bilham, R., and P. England (2001), Plateau "pop-up" in the great 1897 Assam earthquake, *Nature*, *410*(6830), 806–809.

Bilham, R., R. Bendick, and K. Wallace (2003), Flexure of the Indian plate and intraplate earthquakes, *Proc. Indian Acad. Sci. Earth Planet. Sci.*, *112*(3), 315–329.

Biswas, S., and B. Grasemann (2005), Quantitative morphotectonics of the southern Shillong Plateau (Bangladesh/India), *Aust. J. Earth Sci.*, *97*, 82–93.

Bookhagen, B., R. C. Thiede, and M. R. Strecker (2005), Abnormal Monsoon Years (AMYs) and their control on erosion and sediment flux in the high, arid northwest Himalaya, *Earth Planet. Sci. Lett.*, *231*, 131–146.

Boyce, J. W., K. V. Hodges, W. J. Olszewski, and M. J. Jercinovic (2006), He diffusion in monazite: Implications for (U-Th)/He thermochronometry, *Geochem. Geophys. Geosyst.*, *6*, Q12004, doi:10.1029/2005GC001058.

Chakraborty, A. (1972), On the rock stratigraphy and tectonics of the sedimentary belt in the southwest of the Shillong Plateau, Meghalaya, *Oil Nat. Gas Comm. Bull.*, *9*, 133–141.

Chatterjee, N., A. C. Mazumdarb, A. A. Bhattacharya, and R. R. Saikia (2007), Mesoproterozoic granulites of the Shillong-Meghalaya Plateau: Evidence of westward continuation of the Prydz Bay Pan-African suture into Northeastern India, *Precambrian Res.*, *152*, 1–26.

Coffin, M. F., M. S. Pringle, R. A. Duncan, T. P. Gladczenko, M. Storey, R. D. Müller, and G. L. A. (2002), Kerguelen hotspot magma output since 130 Ma, *J. Petrol.*, *43*, 1121–1139.

Copley, A., and D. McKenzie (2007), Models of crustal flow in the India-Asia collision zone, *Geophys. J. Int.*, *169*, 683–698, doi:610.1111/j.1361246X.2007.03343.x.

Das Gupta, A. B., and A. K. Biswas (2000), *Geology of Assam*, 169 pp., Geol. Soc. of India, Bangalore.

Desikachar, S. V. (1974), A review of the tectonic and geological history of eastern India in terms of plate tectonics theory, *J. Geol. Soc. India*, *15*, 137–149.

Dettman, D. L., M. J. Kohn, J. Quade, F. J. Ryerson, P. Tank, T. P. Ojha, and S. Hamidullah (2001), Seasonal stable isotope evidence for a strong Asian monsoon throughout the past 10.7 m.y., *Geology*, *29*, 31–34.

Dettman, D. L., X. M. Fang, C. N. Garzione, and J. J. Li (2003), Uplift-driven climate change at 12 Ma: A long delta O^{18} record from the NE margin of the Tibetan plateau, *Earth Planet. Sci. Lett.*, *214*, 267–277.

de Wit, M. J., S. A. Bowring, L. D. Ashwal, L. G. Randrianasolo, V. P.I. Morel, and R. A. Rambeloson (2001), Age and tectonic evolution of Neoproterozoic ductile shear zones in southwestern Madagascar, with implications for Gondwana studies, *Tectonics*, *20*(1), 1–45.

Donelick, R. A., R. A. Ketcham, and W. D. Carlson (1999), Variability of apatite fission-track annealing kinetics; II, Crystallographic orientation effects, *Am. Mineral.*, *84*(9), 1224–1234.

Donelick, R. A., P. B. O'Sullivan, and R. A. Ketcham (2005), Apatite fission-track analysis, in *Low-Temperature Thermochronology: Techniques, Interpretations, and Applications*, *Rev. Mineral. Geochem.*, vol. 58, edited by P. W. Reiners and T. A. Ehlers, pp. 49–94, Mineral. Soc. of Am., Washington, D. C.

Dumitru, T. A. (1993), A new computer-automated microscope stage system for fission-track analysis, *Nucl. Tracks Radiat. Meas.*, *21*(4), 575–580.

Dunkl, I. (2002), Trackkey: A windows program for calculation and graphical presentation of fission track data, *Comput. Geosci.*, *28*(1), 3–12.

Ehlers, T. A., and K. A. Farley (2003), Apatite (U-Th)/He thermochronometry: Methods and applications to problems in tectonic and surface processes, *Earth Planet. Sci. Lett.*, *206*, 1–14.

Ehlers, T. A., et al. (2005), Computational tools for low-temperature thermochronometer interpretation, in *Low-Temperature Thermochronology: Techniques, Interpretations, and Applications*, *Rev. Mineral. Geochem.*, vol. 58, edited by P. W. Reiners and T. A. Ehlers, pp. 589–622, Mineral. Soc. of Am., Washington, D. C.

England, P., and P. Molnar (1990), Surface uplift, uplift of rocks, and exhumation of rocks, *Geology*, *18*, 1173–1177.

Evans, P. (1964), The tectonic framework of Assam, *J. Geol. Soc. India*, *5*, 80–96.

Farley, K. A. (2002), (U-Th)/He dating: Techniques, calibrations, and applications, in *Noble Gases in Geochemistry and Cosmochemistry*, edited by D. Porcelli, C. J. Ballentine, and R. Wieler, pp. 819–844, Mineral. Soc. of Am., Washington, D. C.

Farley, K. A., and D. F. Stockli (2002), (U-Th)/He dating of Phosphates: Apatite, Monazite, and Xenotime, in *Phosphates*, edited by M. Kohn, M. K. Rakovan, and J. M. Hughes, pp. 559–578, Mineral. Soc. of Am., Washington, D. C.

Farley, K. A., R. Wolf, and L. Silver (1996), The effect of a long alpha-stopping distances on (U-Th)/He dates, *Geochim. Cosmochim. Acta*, *60*, 4223–4229.

Farley, K. A., M. E. Rusmore, and S. W. Bogue (2001), Post-10 Ma uplift and exhumation of the northern Coast Mountains, British Columbia, *Geology*, *29*, 99–102.

Flowers, R. M., S. A. Bowring, and P. W. Reiners (2006), Low long-term erosion rates and extreme continental stability documented by ancient (U-Th)/He dates, *Geology*, *34*, 925–928, doi:910.1130/G22670A.22671.

Gansser, A. (1983), *Geology of the Bhutan Himalaya*, 181 pp., Birkhäuser Verlag, Basel, Switzerland.

Garzanti, E., G. Vezzoli, S. Andò, C. France-Lanord, S. K. Singh, and G. Foster (2004), Sand petrology and focused erosion in collision orogens: The Brahmaputra case, *Earth Planet. Sci. Lett.*, *220*, 157–174.

Ghosh, S., S. Chakraborty, J. K. Bhalla, D. K. Paul, A. Sarkar, P. K. Bishui, and S. N. Gupta (1991), Geochronology and geochemistry of granite plutons from East Khasi Hills, Meghalaya, *J. Geol. Soc. India*, *37*, 331–342.

Ghosh, S., S. Chakraborthy, D. K. Paul, J. K. Bhalla, P. K. Bishui, and S. N. Gupta (1994), New Rb-Sr ages and geochemistry of granitoids from Meghalaya and their significance in middle-late Proterozoic crustal evolution, *Indian Miner.*, *48*, 33–44.

Gleadow, A. J. W., and I. Duddy (1981), A natural long term annealing experiment for apatite, *Nucl. Tracks Radiat. Meas.*, *5*, 169–174.

Green, P. F., I. R. Duddy, A. J. W. Gleadow, and P. R. Tingate (1985), Fission track annealing in apatite: Track length measurements and the form of the Arrhenius plot, *Nucl. Tracks Radiat. Meas.*, *10*, 323–328.

Green, P. F., I. R. Duddy, A. J. W. Gleadow, P. R. Tingate, and G. M. Laslett (1986), Thermal annealing of fission tracks in apatite, 1. A qualitative description, *Chem. Geol.*, *59*, 237–253.

Green, P. F., P. V. Crowhurst, I. R. Duddy, P. Japsen, and S. P. Holford (2006), Conflicting (U-Th)/He and fission track ages in apatite: Enhanced He retention, not anomalous annealing behaviour, *Earth Planet. Sci. Lett.*, *250*, 407–427.

Grujic, D., I. Coutand, B. Bookhagen, S. Bonnet, A. Blythe, and C. Duncan (2006), Climatic forcing of erosion, landscape and tectonics in the Bhutan Himalayas, *Geology*, *34*, 801–804, doi:810.1130/G22648.22641.

Gupta, R. P., and A. K. Sen (1988), Imprints of the Ninety-East Ridge in the Shillong Plateau, Indian Shield, *Tectonophysics*, *154*, 335–341.

Hendriks, B. W. H., and T. F. Redfield (2005), Apatite fission track and (U-Th)/He data from Fennoscandia: An example of underestimation of fission track annealing in apatite, *Earth Planet. Sci. Lett.*, *236*, 443–458.

Hiller, K., and M. Elahi (1984), Structural development and hydrocarbon entrapment in the Surma Basin, Bangladesh (Northwest Indo-Burman Fold Belt), paper presented at 5th Offshore Southeast Asia Conference, Offshore Southeast Asia Pte. Ltd., Singapore.

Hourigan, J. K., P. W. Reiners, and M. T. Brandon (2005), U-Th zonation-dependent alpha-ejection in (U-Th)/He chronometry, *Geochim. Cosmochim. Acta*, *69*, 3349–3365.

House, M. A., B. P. Wernicke, and K. A. Farley (2001), Paleo-geomorphology of the Sierra Nevada, California, from (U-Th)/He ages in apatite, *Am. J. Sci.*, *301*, 77–102.

Jade, S. (2004), Estimates of plate velocity and crustal deformation in the Indian subcontinent using GPS geodesy, *Curr. Sci.*, *86*(10), 1443–1448.

Jauhri, A. K., and K. K. Agarwal (2001), Early Palaeogene in the south Shillong Plateau, NE India: Local biostratigraphic signals of global tectonic and oceanic changes, *Palaeogeogr. Palaeoclimatol. Palaeoecol.*, *168*, 187–203.

Johnson, S. Y., and A. M. N. Alam (1991), Sedimentation and tectonics of the Sylhet trough, Bangladesh, *Geol. Soc. Am. Bull.*, *103*, 1513–1527.

Kayal, J. R., S. S. Arefiev, S. Barua, D. Hazarika, N. Gogoi, A. Kumar, S. N. Chowdhury, and S. Kalita (2006), Shillong plateau earthquakes in northeast India region: Complex tectonic model, *Curr. Sci.*, *91*(1), 109–114.

Kent, R. W., M. S. Pringle, R. D. Müller, A. D. Saunders, and N. C. Ghose (2002), $^{40}Ar/^{39}Ar$ geochronology of the Rajmahal Basalts, India, and their relationship to the Kerguelen plateau, *J. Petrol.*, *43*, 1141–1153.

Ketcham, R. A. (2005), Forward and inverse modeling of low-temperature thermochronometry data, in *Low-Temperature Thermochronology: Techniques, Interpretations, and Applications*, *Rev. Mineral. Geochem.*, vol. 58, edited by P. W. Reiners and T. A. Ehlers, pp. 275–314, Mineral. Soc. of Am., Washington, D. C.

Ketcham, R. A., R. A. Donelick, and W. D. Carlson (1999), Variability of apatite fission-track annealing kinetics; III, Extrapolation to geological time scales, *Am. Mineral.*, *84*(9), 1235–1255.

Ketcham, R. A., R. A. Donelick, and M. B. Donelick (2000), AFTSolve: A program for multi-kinetic modeling of apatite fission-track data, *Geol. Mater. Res.*, *2*(1), 1–32.

Laslett, G. M., and R. F. Galbraith (1996), Statistical modelling of thermal annealing of fission tracks in apatite, *Geochim. Cosmochim. Acta*, *60*, 5117–5131.

Laslett, G. M., P. F. Green, I. R. Duddy, and A. J. W. Gleadow (1987), Thermal annealing of fission tracks in apatite; 2, A quantitative analysis, *Chem. Geol.*, *65*, 1–13.

Mamallan, R., A. B. Awati, S. N. Kak, and K. R. Gupta (1995), Effective utilization of geomorphology in uranium exploration: A success story from Meghalaya, northeast India, *Curr. Sci.*, *68*(11), 11,137–11,140.

Meesters, A. G. C. A., and T. J. Dunai (2002), Solving the production-diffusion equation for finite diffusion domains of various shapes. Part II. Application to cases with (-ejection and nonhomogeneous distribution of the source, *Chem. Geol.*, *186*, 347–363.

Mishra, U. K., and S. Sen (2001), Dinosaur bones from Meghalaya, *Curr. Sci.*, *80*(8), 1053–1056.

Mitra, S. K., and S. C. Mitra (2001), Tectonic setting of the Precambrian of the north-eastern India (Meghalaya Plateau) and age of the Shillong Group of rocks, *Spec. Publ. Geol. Surv. India*, *64*, 653–658.

Mitra, S., K. Priestley, A. K. Bhattacharyya, and V. K. Gaur (2005), Crustal structure and earthquake focal depths beneath northeastern India and southern Tibet, *Geophys. J. Int.*, *160*, 227–248, doi:210.1111/j.1365-1246X.2004.02470.x.

Naeser, C. W. (1976), Fission track dating, *U. S. Geol. Surv. Open File Rep., 76-190*, 65 pp.

Najman, Y. (2006), The detrital record of orogenesis: A review of approaches and techniques used in the Himalayan sedimentary basins, *Earth Sci. Rev.*, *74*, 1–72.

Nandy, D. R. (1980), Tectonic patterns in northeastern India, *Indian J. Earth Sci.*, *7*, 103–107.

Nasdala, L., P. W. Reiners, J. I. Garver, A. K. Kennedy, R. A. Stern, E. Balan, and R. Wirth (2004), Incomplete retention of radiation damage in zircon from Sri Slanka, *Am. Mineral.*, *89*, 219–231.

Oldham, R. D. (1899), Report of the great earthquake of 12th June 1897, *Mem. Geol. Surv. India*, *29*, 1–379.

Panneer Selvan, A., R. N. Prasad, R. Dhana Raju, and R. M. Sinha (1995), Rb–Sr age of the metaluminous granitoids of South Khasi Batholith, Meghalaya: Implications on its genesis and Pan-African activity in northeastern India, *J. Geol. Soc. India*, *46*, 619–624.

Paul, J., et al. (2001), The motion and active deformation of India, *Geophys. Res. Lett.*, *28*(4), 647–651.

Rajendran, C. P., K. Rajendran, B. P. Duarah, S. Baruah, and A. Earnest (2004), Interpreting the style of faulting and paleoseismicity associated with the 1897 Shillong, northeast India, earthquake: Implications for regional tectonism, *Tectonics*, *23*, TC4009, doi:10.1029/2003TC001605.

Rao, R. U. M., G. V. Rao, and H. Narain (1976), Radioactive heat generation and heat flow in the Indian shield, *Earth Planet. Sci. Lett.*, *30*, 57–64.

Rath, S., S. K. Singh, and S. C. K. Sarma (1997), Hydrocarbon prospects of the poorly explored north bank of Brahmaputra, north east India, *J. Geophys.*, *18*(3), 159–164.

Ray, J. S., J. R. Trivedi, and A. M. Dayal (2000), Strontium isotope systematics of Amba Dongar and Sung Valley carbonatite-alkaline complexes, India: Evidence for liquid immiscibility, crustal contamination and long-lived Rb/Sr enriched mantle sources, *J. Asian Earth Sci.*, *18*, 585–594.

Reich, M., R. C. Ewing, T. A. Ehlers, and U. Becker (2007), Low-temperature anisotropic diffusion of helium in zircon: Implications for zircon (U-Th)/He thermochronometry, *Geochim. Cosmochim. Acta*, *71*, 3119–3130.

Reiners, P. W. (2005), Zircon (U-Th)/He thermochronometry, in *Low-Temperature Thermochronology: Techniques, Interpretations, and Applications*, *Rev. Mineral. Geochem.*, vol. 58, edited by P. W. Reiners and T. A. Ehlers, pp. 151–179, Mineral. Soc. of Am., Washington, D. C.

Reiners, P. W., and K. A. Farley (1999), Helium diffusion and (U-Th)/He thermochronometry of titanite, *Geochim. Cosmochim. Acta*, *63*, 3845–3859.

Reiners, P. W., and K. A. Farley (2001), Influence of crystal size on apatite (U-Th)/He thermochronology: An example from the Bighorn Mountains, Wyoming, *Earth Planet. Sci. Lett.*, *188*, 413–420.

Reiners, P. W., K. A. Farley, and H. J. Hickes (2002), He diffusion and (U-Th)/He thermochronometry of zircon: Initial results from Fish Canyon Tuff and Gold Butte, Nevada, *Tectonophysics*, *349*, 247–308.

Reiners, P. W., T. L. Spell, S. Nicolescu, and K. A. Zanetti (2004), Zircon (U-Th)/He thermochronometry: He diffusion and comparisons with 40Ar/39Ar dating, *Geochim. Cosmochim. Acta*, *68*, 1857–1887.

Sengupta, S., L. Sangma, D. Ganguly, S. S. Srivastava, and B. Kumar (1998), Geological and mineralogical map of north east India, map, Geol. Surv. of India, Hyderabad.

Shamsuddin, A. K. M., and S. K. M. Abdullah (1997), Geologic evolution of the Bengal Basin and its implication in hydrocarbon exploration in Bangladesh, *Indian J. Geol.*, *69*(2), 93–121.

Shuster, D. L., R. M. Flowers, and K. A. Farley (2006), The influence of natural radiation damage on helium diffusion kinetics in apatite, *Earth Planet. Sci. Lett.*, *249*, 148–161.

Singh, C. S., A. K. Khana, and S. N. Singh (1998), Seismic velocities for effective planning of exploratory well in virgin area—A case from north bank areas of Upper Assam, *J. Geophys.*, *19*(2), 101–107.

Sobel, E. R., and M. R. Strecker (2003), Uplift, exhumation and precipitation: Tectonic and climatic control of Late Cenozoic landscape evolution in the northern Sierras Pampeanas, Argentina, *Basin Res.*, *15*, doi:10.1046/j.1365-2117.2003.00214.x.

Socquet, A., C. Vigny, N. Chamot-Rooke, W. Simons, C. Claude Rangin, and B. Ambrosius (2006), India and Sunda plates motion and deformation along their boundary in Myanmar determined by GPS, *J. Geophys. Res.*, *111*, B05406, doi:10.1029/2005JB003877.

Srivastava, R. K., L. M. Heaman, A. K. Sinha, and S. Shihua (2005), Emplacement age and isotope geochemistry of Sung Valley alkaline-carbonatite complex, Shillong Plateau, northeastern India: Implications for primary carbonate melt and genesis of the associated silicate rocks, *Lithos*, *81*, 33–54.

Stockli, D. F. (2005), Application of low-temperature thermochronometry to extensional tectonic settings, in *Low-Temperature Thermochronology: Techniques, Interpretations, and Applications*, *Rev. Mineral. Geochem.*, vol. 58, edited by P. W. Reiners and T. A. Ehlers, pp. 411–448, Mineral. Soc. of Am., Washington, D. C.

Stockli, D. F., and K. A. Farley (2004), Empirical constraints on the titanite (U-Th)/He partial retention zone from the KTB drill hole, *Chem. Geol.*, *207*, 223–236.

Stockli, D. F., K. A. Farley, and T. A. Dumitru (2000), Calibration of the apatite (U-Th)/He thermochronometer on an exhumed fault block, White Mountains, California, *Geology*, *28*, 983–986.

Tagami, T., and P. B. O'Sullivan (2005), Fundamentals of fission-track thermochronology, in *Low-Temperature Thermochronology: Techniques, Interpreta-*

tions, and Applications, *Rev. Mineral. Geochem.*, vol. 58, edited by P. W. Reiners and T. A. Ehlers, pp. 19–47, Mineral. Soc. of Am., Washington, D. C.

Tagami, T., K. A. Farley, and D. F. Stockli (2003), Thermal sensitivities of zircon (U-Th)/He and fission-track systems, paper presented at 13th Annual Goldschmidt V.M. Conference, Kyoto, Japan.

Uddin, A., and N. Lundberg (1999), A paleo-Brahmaputra? Subsurface lithofacies analysis of Miocene deltaic sediments in the Himalyan-Bengal system, Bangladesh, *Sediment. Geol.*, *123*, 239–254.

Uddin, A., and N. Lundberg (2004), Miocene sedimentation and subsidence during continent-continent collision, Bengal basin, Bangladesh, *Sediment. Geol.*, *164*, 131–146.

USGS-Bangladesh Gas Assessment Team (2001), *U.S. Geological Survey-PetroBangla Cooperative Assessment of Undiscovered Natural Gas Resources of Bangladesh*, 119 pp, U.S. Geol. Surv., Denver, Colo.

van Breeman, O., D. R. Bowes, C. C. Bhattacharjee, and P. K. Chowdhary (1989), Late Proterozoic-Early Palaeozoic Rb-Sr wholerock and mineral ages for granite and pegmatite, Goalpara, Assam, India, *J. Geol. Soc. India*, *33*, 89–92.

Veena, K., B. K. Pandey, P. Krishnamurthy, and J. N. Gupta (1988), Pb, Sr and Nd isotopic systematics of the carbonatites of Sung Valley, Meghalaya, northeast India: Implications for contemporary plume-related mantle source characteristics, *J. Petrol.*, *39*, 1875–1884.

Veevers, J. J. (2006), Updated Gondwana (Permian-Cretaceous) Earth history of Australia, *Gondwana Res.*, *9*(3), 231–260.

Veevers, J. J., and R. C. Tewari (1995), *Gondwana Master Basin of Peninsular India Between Tethys and the Interior of the Gondwanaland Province of Pangea*, Geol. Soc. of Am., Boulder, Colo.

Wolf, R. A., K. A. Farley, and D. M. Kass (1998), Modeling of the temperature sensitivity of the apatite (U-Th)/He thermochronometer, *Chem. Geol.*, *148*, 105–114.

Worm, H.-U., A. M. M. Ahmed, N. U. Ahmed, H. O. Islam, M. M. Huq, U. Hambach, and J. Lietz (1998), Large sedimentation rate in the Bengal Delta: Magnetostratigraphic dating of Cenozoic sediments from northeastern Bangladesh, *Geology*, *26, 487–490.*

Zahid, K. M., and A. Uddin (2005), Influence of overpressure on formation velocity evaluation of Neogene strata from the eastern Bengal Basin, Bangladesh, *J. Asian Earth Sci.*, *25*, 419–429.

Zhang, P. Z., et al. (2004), Continuous deformation of the Tibetan Plateau from global positioning system data, *Geology*, *32*, 809–812, doi:810.1130/G20554.20551.

S. Biswas, Department of Geological Sciences, Jahangirnagar University, Savar, Dhaka 1342, Bangladesh. (biswas.subrata@gmail.com)

I. Coutand, UMR-CNRS 8110, Processus et Bilans des Domaines Sédimentaires, Université des Sciences et Technologies de Lille 1, F-59655 Villeneuve d'Ascq Cedex, France. (isabelle.coutand@univ-lille1.fr)

B. Grasemann, Center for Earth Sciences, University of Vienna, Althanstrasse 14, A-1090 Vienna, Austria. (bernhard.grasemann@univie.ac.at)

D. Grujic, Department of Earth Sciences, Dalhousie University, Halifax, NS, Canada B3H 4J1. (dgrujic@dal.ca)

C. Hager and D. Stöckli, Department of Geology, University of Kansas, Lawrence, KS 66045-7613, USA. (hager@ku.edu; stockli@ku.edu)